FERMILAB-PUB-23-368-ND

Measurement of three-dimensional inclusive muon-neutrino charged-current cross sections on argon with the MicroBooNE detector

P. Abratenko[aj], O. Alterkait[aj], D. Andrade Aldana[1], L. Arellano[t], J. Asaadi[ai], A. Ashkenazi[ag], S. Balasubramanian[l], B. Baller[l], G. Barr[z], D. Barrow[z], J. Barrow[ag,u], V. Basque[l], O. Benevides Rodrigues[1,af], S. Berkman[l], A. Bhanderi[t], A. Bhat[g], M. Bhattacharya[l], M. Bishai[c], A. Blake[q], B. Bogart[v], T. Bolton[p], J. Y. Book[n], L. Camilleri[j], Y. Cao[t], D. Caratelli[d], I. Caro Terrazas[i], F. Cavanna[l], G. Cerati[l], Y. Chen[ac], J. M. Conrad[u], M. Convery[ac], L. Cooper-Troendle[aa,an], J. I. Crespo-Anadón[f], M. Del Tutto[l], S. R. Dennis[e], P. Detje[e], A. Devitt[q], R. Diurba[b], Z. Djurcic[a], R. Dorrill[o], K. Duffy[z], S. Dytman[aa], B. Eberly[ae], P. Englezos[ab], A. Ereditato[l,g], J. J. Evans[t], R. Fine[r], O. G. Finnerud[t], W. Foreman[1], B. T. Fleming[g], N. Foppiani[n], D. Franco[g], A. P. Furmanski[w], D. Garcia-Gamez[m], S. Gardiner[l], G. Ge[j], S. Gollapinni[r,ah], O. Goodwin[t], E. Gramellini[l,t], P. Green[z], H. Greenlee[l], W. Gu[c], R. Guenette[t], P. Guzowski[t], L. Hagaman[g], O. Hen[u], R. Hicks[r], C. Hilgenberg[w], G. A. Horton-Smith[p], Z. Imani[aj], B. Irwin[w], R. Itay[ac], C. James[l], X. Ji[c,x], L. Jiang[al], J. H. Jo[c], R. A. Johnson[h], Y.-J. Jwa[j], D. Kalra[j], N. Kamp[u], G. Karagiorgi[j], W. Ketchum[l], M. Kirby[l], T. Kobilarcik[l], I. Kreslo[b], M. B. Leibovitch[d], I. Lepetic[ab], J.-Y. Li[k], K. Li[an], Y. Li[c], K. Lin[ab], B. R. Littlejohn[1], H. Liu[c], W. C. Louis[r], X. Luo[d], C. Mariani[al], D. Marsden[t], J. Marshall[am], N. Martinez[p], D. A. Martinez Caicedo[ad], A. Mastbaum[ab], N. McConkey[ak], V. Meddage[p], J. Micallef[aj,u], K. Miller[g], A. Mogan[i], T. Mohayai[l], M. Mooney[i], A. F. Moor[e], C. D. Moore[l], L. Mora Lepin[t], M. M. Moudgalya[t], S. Mulleriababu[b], D. Naples[aa], A. Navrer-Agasson[t], N. Nayak[c], M. Nebot-Guinot[k], J. Nowak[q], N. Oza[j], O. Palamara[l], N. Pallat[w], V. Paolone[aa], A. Papadopoulou[a], V. Papavassiliou[y], H. B. Parkinson[k], S. F. Pate[y], N. Patel[q], Z. Pavlovic[l], E. Piasetzky[ag], I. D. Ponce-Pinto[an], I. Pophale[q], S. Prince[n], X. Qian[c], J. L. Raaf[l], V. Radeka[c], A. Rafique[a], M. Reggiani-Guzzo[t], L. Ren[y], L. Rochester[ac], J. Rodriguez Rondon[ad], M. Rosenberg[aj], M. Ross-Lonergan[r], C. Rudolf von Rohr[b], I. Safa[j], G. Scanavini[an], D. W. Schmitz[g], A. Schukraft[l], W. Seligman[j], M. H. Shaevitz[j], R. Sharankova[l], J. Shi[e], E. L. Snider[l], M. Soderberg[af], S. Söldner-Rembold[t], J. Spitz[v], M. Stancari[l], J. St. John[l], T. Strauss[l], A. M. Szelc[k], W. Tang[ah], N. Taniuchi[e], K. Terao[ac], C. Thorpe[q], D. Torbunov[c], D. Totani[d], M. Toups[l], Y.-T. Tsai[ac], J. Tyler[p], M. A. Uchida[e], T. Usher[ac], B. Viren[c], M. Weber[b], H. Wei[s], A. J. White[g], Z. Williams[ai], S. Wolbers[l], T. Wongjirad[aj], M. Wospakrik[l], K. Wresilo[e], N. Wright[u], W. Wu[l], E. Yandel[d], T. Yang[l], L. E. Yates[l], H. W. Yu[c], G. P. Zeller[l], J. Zennamo[l], C. Zhang[c],

(The MicroBooNE Collaboration)*

[a]*Argonne National Laboratory (ANL), Lemont, IL, 60439, USA*
[b]*Universität Bern, Bern CH-3012, Switzerland*
[c]*Brookhaven National Laboratory (BNL), Upton, NY, 11973, USA*
[d]*University of California, Santa Barbara, CA, 93106, USA*
[e]*University of Cambridge, Cambridge CB3 0HE, United Kingdom*
[f]*Centro de Investigaciones Energéticas, Medioambientales y Tecnológicas (CIEMAT), Madrid E-28040, Spain*
[g]*University of Chicago, Chicago, IL, 60637, USA*
[h]*University of Cincinnati, Cincinnati, OH, 45221, USA*
[i]*Colorado State University, Fort Collins, CO, 80523, USA*
[j]*Columbia University, New York, NY, 10027, USA*

[k]University of Edinburgh, Edinburgh EH9 3FD, United Kingdom
[l]Fermi National Accelerator Laboratory (FNAL), Batavia, IL 60510, USA
[m]Universidad de Granada, Granada E-18071, Spain
[n]Harvard University, Cambridge, MA 02138, USA
[o]Illinois Institute of Technology (IIT), Chicago, IL 60616, USA
[p]Kansas State University (KSU), Manhattan, KS, 66506, USA
[q]Lancaster University, Lancaster LA1 4YW, United Kingdom
[r]Los Alamos National Laboratory (LANL), Los Alamos, NM, 87545, USA
[s]Louisiana State University, Baton Rouge, LA, 70803, USA
[t]The University of Manchester, Manchester M13 9PL, United Kingdom
[u]Massachusetts Institute of Technology (MIT), Cambridge, MA, 02139, USA
[v]University of Michigan, Ann Arbor, MI, 48109, USA
[w]University of Minnesota, Minneapolis, MN, 55455, USA
[x]Nankai University, Nankai District, Tianjin 300071, China
[y]New Mexico State University (NMSU), Las Cruces, NM, 88003, USA
[z]University of Oxford, Oxford OX1 3RH, United Kingdom
[aa]University of Pittsburgh, Pittsburgh, PA, 15260, USA
[ab]Rutgers University, Piscataway, NJ, 08854, USA
[ac]SLAC National Accelerator Laboratory, Menlo Park, CA, 94025, USA
[ad]South Dakota School of Mines and Technology (SDSMT), Rapid City, SD, 57701, USA
[ae]University of Southern Maine, Portland, ME, 04104, USA
[af]Syracuse University, Syracuse, NY, 13244, USA
[ag]Tel Aviv University, Tel Aviv, Israel, 69978
[ah]University of Tennessee, Knoxville, TN, 37996, USA
[ai]University of Texas, Arlington, TX, 76019, USA
[aj]Tufts University, Medford, MA, 02155, USA
[ak]University College London, London WC1E 6BT, United Kingdom
[al]Center for Neutrino Physics, Virginia Tech, Blacksburg, VA, 24061, USA
[am]University of Warwick, Coventry CV4 7AL, United Kingdom
[an]Wright Laboratory, Department of Physics, Yale University, New Haven, CT, 06520, USA

Abstract

We report the measurement of the differential cross section $d^2\sigma(E_\nu)/d\cos(\theta_\mu)dP_\mu$ for inclusive muon-neutrino charged-current scattering on argon. This measurement utilizes data from 6.4×10^{20} protons on target of exposure collected using the MicroBooNE liquid argon time projection chamber located along the Fermilab Booster Neutrino Beam with a mean neutrino energy of approximately 0.8 GeV. The mapping from reconstructed kinematics to truth quantities, particularly from reconstructed to true neutrino energy, is validated within uncertainties by comparing the distribution of reconstructed hadronic energy in data to that of the model prediction in different muon scattering angle bins after applying a conditional constraint from the muon momentum distribution in data. The success of this validation gives confidence that the missing energy in the MicroBooNE detector is well-modeled within uncertainties in simulation, enabling the unfolding to a three-dimensional measurement over muon momentum, muon scattering angle, and neutrino energy. The unfolded measurement covers an extensive phase space, providing a wealth of information useful for future liquid argon time projection chamber experiments measuring neutrino oscillations. Comparisons against a number of commonly used model predictions are included and their performance in different parts of the available phase-space is discussed.

Keywords: neutrino experiment, neutrino cross-section, charged-current interactions

Precision modeling of neutrino-nucleus interactions is necessary to achieve the goals of future accelerator neutrino oscillation experiments. Neutrino cross-section modeling is one of the dominant sources of uncertainty in the current generation of oscillation experiments [1, 2] and could in principle limit the search for leptonic charge-parity violation [3, 4]. In the energy range of 0.1–5 GeV, the dominant modes of neutrino interactions, such as quasi-elastic (QE) scattering and resonance production, are difficult to model because of various nuclear effects. Typical examples include nuclear ground state modeling, nucleon-nucleon correlations, and final state interactions [5]. Efforts to simulate these interactions accurately would benefit from dedicated measurements that probe the combined phase space of leptonic and hadronic kinematics. For inclusive muon neutrino (ν_μ) charged current (CC) scattering, there are three degrees of freedom determining the principle interaction kinematics: the scattering muon momentum (P_μ) and angle (θ_μ) that are directly measured, and the neutrino energy (E_ν) that is deduced with the measurement of the hadronic energy. The accurate reconstruction of the neutrino energy is of particular importance to upcoming precision long-baseline neutrino oscillation measurements [6, 7].

There have been continuous advancements in the field of inclusive and exclusive neutrino-nucleus scattering (see Ref. [8, 9, 10, 11, 12, 13] among others for recent progress). Of particular interest to the measurement presented in this article is a recent triple-differential cross section measured on carbon at MINERνA, where the independent variables are the muon kinematics and the total observed proton energy [14]. On an argon target, single- and double-differential ν_μ CC inclusive cross sections have been reported [15, 16, 17, 18]. The measurement presented here expands upon the work measuring energy-dependent cross sections in Ref. [18]. Specifically, we report the first measurement of the nominal-flux-averaged inclusive ν_μ CC double-differential cross section on argon as a function of neutrino energy $d^2\sigma(E_\nu)/d\cos(\theta_\mu)dP_\mu$. Neutrino events are selected using the ν_μ selection described in [19], with $E_\nu \in [0.2, 4.0]$ GeV and $P_\mu \in [0, 2.5]$ GeV/c, giving an overall selection efficiency of 68% and purity of 92%. The estimation of the neutrino energy uses measurements of the visible hadronic energy ($E^{\rm rec}_{\rm had}$) and reconstructed muon momentum ($P^{\rm rec}_\mu$). Thanks to high statistics in this sample and comprehensive coverage of the three-dimensional phase space, we extend the validation procedure first presented in [18] from single to multiple dimensions. The procedure works by comparing reconstructed distributions in data with the corresponding model prediction through the use of χ^2 goodness-of-fit test statistics to demonstrate that the model uncertainties cover the difference between data and prediction. The comparison over the hadronic energy distribution is enhanced by using the muon kinematics measurement as a constraint on the model prediction, providing a more stringent test that is sensitive to the modeling of missing hadronic energy.

The MicroBooNE liquid argon time projeciton chamber (LArTPC) measures 2.56 m along the drift direction, 10.36 m along the beam direction, and 2.32 m along the vertical direction. It has an active mass of 85 tonnes of LAr and is capable of mm-level position resolution, as well as calorimetry with MeV-level detection threshold [20]. Ionization electrons drift in a 273 V/cm electric field towards an anode consisting of 3 detection planes of wires at 60° angles to each other with a wire pitch of 3 mm. Thirty-two photomultiplier tubes (PMTs) are used to detect the scintillation light from the interaction to provide a prompt timing signal. The Booster Neutrino Beam (BNB) at Fermilab produces neutrinos at a target 470 m upstream of the MicroBooNE detector, with 93.6% estimated to be ν_μ at a mean E_ν of 0.8 GeV [21].

The event selection used in this analysis is the same as the ν_μ CC selection used in the MicroBooNE inclusive ν_e low-energy excess search [19], and was performed on a data set collected

---

[*] microboone_info@fnal.gov

from 2016–2018 using an exposure of 6.4×10^{20} protons on target (POT), an order of magnitude larger than the single-differential energy-dependent cross section measurement presented in [18]. The Wire-Cell reconstruction chain leverages the detector information through the use of tomography, matching of TPC-charge clusters to PMT-light flashes, and trajectory fitting for particle identification and cosmic-ray removal [22, 23]. Higher-level algorithms perform pattern recognition, neutrino vertex identification, topology classification, and particle identification to produce a particle flow within an event [24]. The boosted-decision-tree library XGBoost [25] is then used to further reduce backgrounds to achieve the ν_μ CC selection.

Energy reconstruction is crucial for the extraction of energy-dependent cross sections [18] as well as for the search for new physics beyond the Standard Model [19]. Generally, energy reconstruction is separated into the reconstruction of particle tracks and of electromagnetic (EM) showers. By default, particle tracks have their energy estimated from their propagation length using a tabulation of the Bethe-Bloch formula from the NIST PSTAR database [26]. This method is substituted with a calorimetry-based approach in cases where the range-based estimation is poor, including short tracks ($< 4\,\mathrm{cm}$), tracks exiting the detector, tracks that frequently change directions, and muon tracks with identified δ rays [24]. The calorimetry-based approach uses a recombination model [27] to convert the measured dQ/dx to the energy loss per unit length dE/dx, which is then integrated. The estimation of EM shower energy also follows a calorimetry-based approach, but uses the total measured charge and a different scale factor [28] that includes the overall mean recombination effect as well as contributions for clustering efficiency and detection threshold. This scaling factor is validated through the reconstructed invariant mass of the neutral pion [29]. Reconstructed muons, charged pions, and electron candidates have their mass added to their energy reconstruction, and proton candidates are assigned an average binding energy of 8.6 MeV [30]. The reconstructed neutrino energy is constructed as the sum of the muon and hadronic energies. Energy resolutions are estimated from Monte Carlo simulation [31]. For ν_μ CC events with their main TPC cluster fully contained within the fiducial volume (fully contained events), the estimated kinematic resolutions are ≈10% on muon energy, ≈30–50% on energy transfer, defined as $E_\nu - E_\mu$, resulting from imperfect reconstruction and missing hadronic energy $E_{\mathrm{had}}^{\mathrm{missing}}$, and ≈20% on E_ν. The angular resolution reaches 5° in θ_μ at forward angles, but is less accurate at backwards angles.

The neutrino flux prediction is derived from the MiniBooNE flux simulation [21] updated to the MicroBooNE detector location, with muon neutrino flux prediction uncertainties ranging from 5–15% over the flux range of ≈0.1–4.0 GeV. Neutrino-argon (ν-Ar) interactions are modeled using `GENIE` v3.0.6 G18_10a_02_11a tuned to T2K data [31, 32], referred to as the `MicroBooNE model`. In particular, hadronic interactions contributing to missing energy are conservatively estimated, with proton-to-neutron conversion and proton knockout having 50% and 20% uncertainties respectively [33]. The model also includes a conservative 50% uncertainty on the 2p2h normalization. Overall, there is a ≈20% ν-Ar interaction uncertainty on the measurement. Measurement uncertainties on flux, cross section, and secondary interactions of protons and charged pions outside the target nucleus (0.6%, simulated with `GEANT4` [34]) are each modeled using a multisim technique to calculate a covariance matrix [35]. Additionally, uncertainties are included for the model simulation statistics that are estimated using the Poisson likelihood method [36] (10%), the modeling of "dirt" events originating outside the cryostat [19] (below 1%), the POT (2%) based on measurements of the originating proton flux [21], and the number of target nuclei (1%). Plots showing the breakdown of total uncertainties by type and the total fractional uncertainties can be found in the supplemental material [37].

The detector response uncertainty considers the same effects as in previous work [38, 18] and takes into account the impact of variations in TPC waveform, light yield and propagation, the space charge effect, and ionization recombination [39, 40, 27]. A fixed set of MC interactions are simulated multiple times, first using parameter central values (CV) and then individually applying a 1σ variation to each parameter. To compensate for limited simulation statistics, re-sampling of events is performed through a bootstrapping procedure, as discussed in Ref. [19]. For each parameter, we compute the average difference vector between the CV and 1σ variation, $\vec{V}_D^{\mathrm{nominal}}$, as well as its estimated covariance M_R. These are used to construct a normal distribution of variations that is repeatedly sampled in the formation of the overall detector response covariance matrix M_D.

Because simulating events and propagating them through the detector is computationally expensive, there is a limited quantity of simulated events available. The large number of bins involved in a three-dimensional analysis leads to a small number of events per bin, causing large statistical fluctuations in $\vec{V}_D^{\mathrm{nominal}}$, and an over-estimation of the covariance in M_R and M_D. To address this, a Gaussian Processes Regression (GPR) smoothing algorithm [41, 42, 43] is applied to the distribution in $\vec{V}_D^{\mathrm{nominal}}$, smoothing the statistical fluctuations introduced by the bootstrapping procedure. GPR uses a Bayesian approach to model the data with a joint Gaussian distribution and an uninformed prior. A smoothed posterior is computed from the simulated values of $\vec{V}_D^{\mathrm{nominal}}$, as well as a kernel matrix Σ_K that asserts our intuition of smoothness between nearby bin centers x_1, x_2 through a radial basis kernel function $K(x_1, x_2) = e^{-|(\vec{x}_1-\vec{x}_2)\cdot\vec{s}|^2/2}$. Based on reconstruction resolutions [24], length scales L_i were chosen to be 0.1 in $\cos(\theta_\mu^{\mathrm{rec}})$ and 20% for each of E_ν^{rec} and P_μ^{rec} to calculate $s_i = 1/L_i$. The supplemental material [37] provides additional details on the implementation of GPR smoothing in this work. The central value and covariance of the posterior prediction are used in place of the original $\vec{V}_D^{\mathrm{nominal}}$ and M_R. Because of GPR smoothing, statistical fluctuations are controlled and become less impactful in M_D, reducing the overall detector response covariance by an order of magnitude to $\approx$20%. The validity of this reduction is tested through the data/simulation goodness-of-fit (GoF) tests.

Since the `MicroBooNE model` is used to estimate the selection efficiency and unfold the reconstructed variables, such as E_ν^{rec}, to truth quantities, it is important to validate its accuracy. If this model (including its uncertainties) is unable to describe the distribution in data, it may introduce significant bias beyond the uncertainties into the extracted cross sections. Therefore, a comprehensive set of data/simulation comparisons using the reconstructed kinematic variables P_μ^{rec}, $\cos(\theta_\mu^{\mathrm{rec}})$, and $E_{\mathrm{had}}^{\mathrm{rec}}$ are investigated and discussed below, demonstrating the validity of the model. Since $E_{\mathrm{had}}^{\mathrm{rec}}$ represents the reconstruction of the visible component of the energy transfer, it is the ideal distribution to study in complement with the muon kinematics, which together account for E_ν.

Because some of the energy in the neutrino interaction may not be reconstructed (e.g. carried away in undetected neutrons and particles below the detection threshold), the mapping from reconstructed to true E_ν needs special attention. This mapping is tested through the combination of GoF tests over the muon kinematics and GoF tests over $E_{\mathrm{had}}^{\mathrm{rec}}$, and the model is only considered to be validated if all tests show χ^2/ndf consistent within a 2σ level of agreement. These first tests investigate the modeling of the muon kinematics as a prerequisite for their use as a constraint on the $E_{\mathrm{had}}^{\mathrm{rec}}$ prediction, and are performed over the two-dimensional (2D) $\{P_\mu^{\mathrm{rec}}, \cos(\theta_\mu^{\mathrm{rec}})\}$ distribution and are shown in the supplemental material [37]. They give χ^2/ndf of 105/144 and 103/144 for the fully and partially contained events respectively, demonstrating that the model is able to describe the distribution of muon kinematics seen in data well within the model uncertainties.

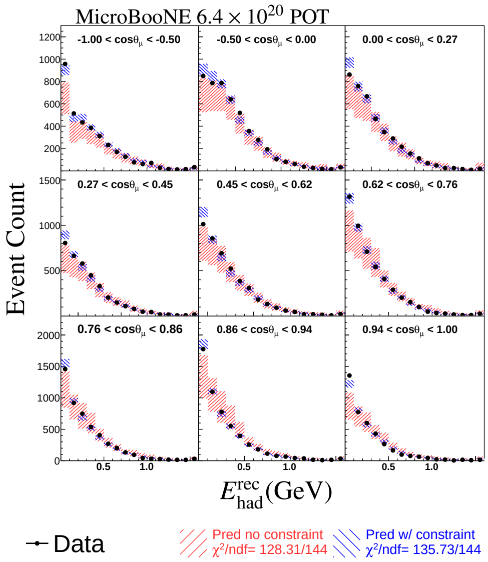

Figure 1: Distribution of data and prediction over the 2D reconstructed binning of $\{E_{\text{had}}^{\text{rec}}, \cos(\theta_{\mu}^{\text{rec}})\}$ for fully contained events (partially contained event distributions are shown in the supplemental material [37]). The `MicroBooNE model` prediction, including before (red) and after (blue) applying the measurement of the data distribution over $\{P_{\mu}^{\text{rec}}, \cos(\theta_{\mu}^{\text{rec}})\}$ as a constraint, is compared to data.

Next, a GoF test is performed over the 2D $\{E_{\text{had}}^{\text{rec}}, \cos(\theta_{\mu}^{\text{rec}})\}$ distribution, shown in Fig. 1, and is constrained by the muon kinematics measurement using the conditional constraint formalism [44], described in more detail in the supplemental material [37]. It demonstrates a χ^2/ndf of 136/144 after applying the constraint, again indicating that the model describes the relationship between $\{P_{\mu}^{\text{rec}}, \cos(\theta_{\mu}^{\text{rec}})\}$ and $\{E_{\text{had}}^{\text{rec}}, \cos(\theta_{\mu}^{\text{rec}})\}$ in data within uncertainties. The constraint highly suppresses the common uncertainties between these distributions, causing the posterior prediction to have much lower uncertainties and leading to a more stringent examination of the model. Through the demonstration of accurate muon kinematics modeling, combined with accurate modeling of $E_{\text{had}}^{\text{rec}}$ in relation to $\{P_{\mu}^{\text{rec}}, \cos(\theta_{\mu}^{\text{rec}})\}$, the GoF tests validate the modeling of the missing hadronic energy to describe the data within uncertainties. This builds confidence that the use of the `MicroBooNE model` in unfolding does not introduce bias beyond the quoted uncertainties.

To help demonstrate the sensitivity of this data-driven model validation approach, a series of fake data studies are performed. One fake dataset is generated using the `NuWro` model prediction, and others are generated by varying the reconstructed proton energy of events simulated using the `MicroBooNE model`. Each fake data study compares the sensitivity in the GoF test χ^2/ndf to the corresponding level of bias in the unfolded measurement when compared to the underlying truth. In all cases, the GoF tests demonstrate higher sensitivity to mismodeling than the extracted measurements show bias from unfolding to the three-dimensional binning used in the analysis. In each of these cases the bias on the unfolded measurement is within the total model uncertainties, and furthermore is either within the cross section and statistical uncertainties or is detected by the GoF test. See the the supplemental material [37] for details on the three-dimensional fake data studies.

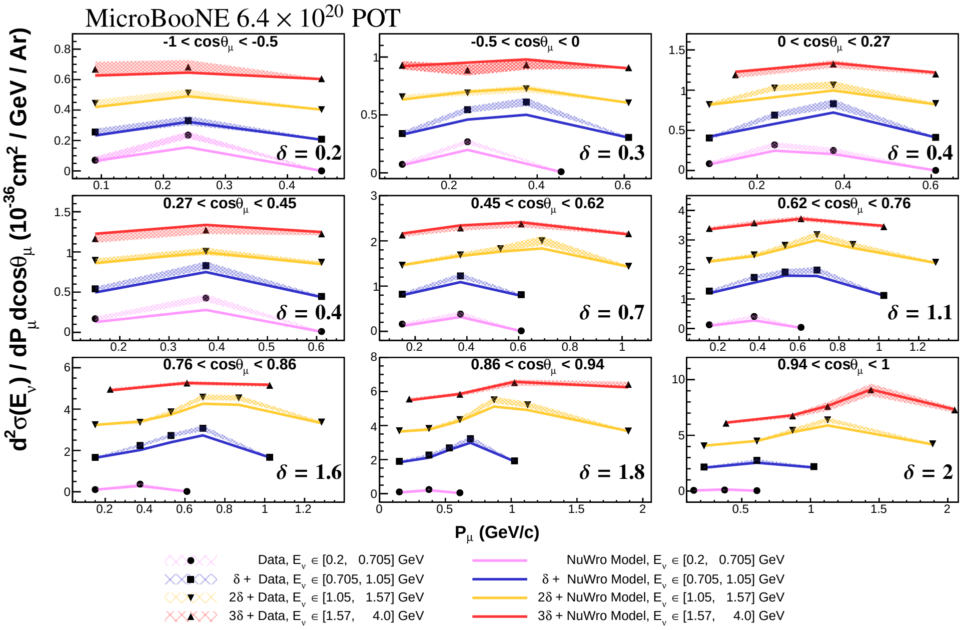

Figure 2: Unfolded measurement of the inclusive ν_μ CC differential cross section on argon and `NuWro` prediction, chosen for having the lowest χ^2, are shown within each angle slice and with each E_ν measurement overlaid and offset to visually separate them. A comparison to the `MicroBooNE model` is given in the supplemental material [37]. The magnitude of the offset δ, given in the same units as the cross section, 10^{-36}cm^2/GeV/Ar, is listed in the bottom right of each plot. Uncertainties on the extracted cross section are shown through the shaded bands.

The three-dimensional cross section is extracted using the Wiener-SVD unfolding technique [45]. A regularization term is constructed from matrices that compute the third derivative of the unfolded distribution with respect to each of E_ν, $\cos(\theta_\mu)$, and P_μ by taking differences of nearby bins, and are further combined in quadrature. The covariance matrix includes statistical uncertainties, computed using the combined Neyman-Pearson method [46], as well as systematic uncertainties for signal and background events. The bias introduced in unfolding and regularization is captured in an additional smearing matrix A_C that is applied to every theoretical prediction reported in this work and included in the data release in the supplemental material [37].

The unfolded cross section consists of 138 bins spanning 4 E_ν slices, 9 $\cos(\theta_\mu)$ slices, and 3–6 P_μ bins within each $\{E_\nu, \cos(\theta_\mu)\}$ slice based on the detector resolution and statistics available. The full differential cross section is shown in Fig. 2, where the 9 windows correspond to increasingly forward-angle slices of $\cos(\theta_\mu)$. Within each window the P_μ distribution is plotted for each of the four E_ν slices, offset by an arbitrary shift (δ) for visual clarity. The data is plotted against the `NuWro 19.02.01` prediction [47], which among the considered generators has the best agreement with the data, as measured by the χ^2 listed in Table 1 and described in more detail in the supplemental material [37].

Table 1 presents comparisons with model predictions for `GENIE v2.12.10` [48] (`GENIE v2`), the `MicroBooNE` model, `GENIE v3.0.6 G18_10a_02_11a` [49] (`GENIE v3 untuned`), `GiBUU 2021` [50] (`GiBUU`), `NEUT 5.4.0.1` [51] (`NEUT`), and `NuWro 19.02.01` [47] (`NuWro`). A comparison of the underlying physics models in these event generators can be found in Ref. [52]. The

Table 1: Comparisons between various models and the unfolded three-dimensional measurement.

Model Name	χ^2/ndf
`GENIE v2`	752.2/138
`MicroBooNE model`	329.3/138
`GENIE v3 untuned`	324.6/138
`GiBUU`	275.2/138
`NEUT`	244.3/138
`NuWro`	214.1/138

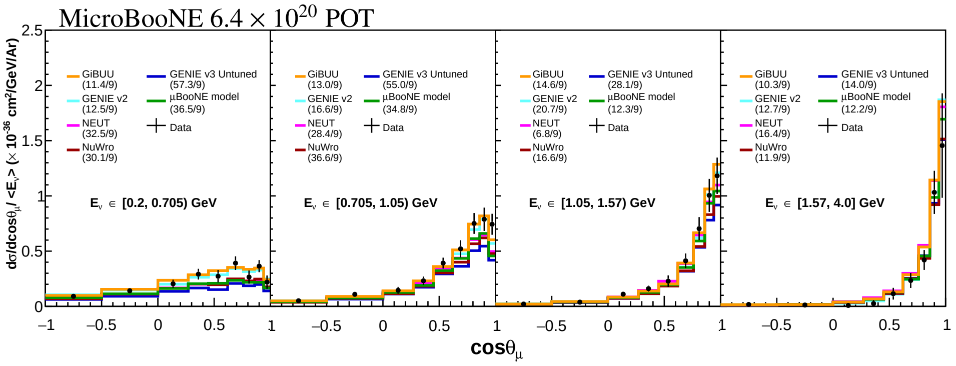

Figure 3: Unfolded measurement of the inclusive ν_μ CC differential cross section on argon over a function of $\cos(\theta_\mu)$ after integrating over P_μ and normalizing by the average $\langle E_\nu \rangle$ in each E_ν bin. Goodness-of-fit χ^2/ndf given with each prediction for the corresponding angle slice. See supplemental material [37] for full table of χ^2 values.

unfolded three-dimensional measurement is found to be in tension with all model CV predictions. `NEUT` and `NuWro` show the best agreement, followed by `GiBUU`, broadly similar to the hierarchy of agreement found previously in the single-differential analysis [18]. Owing to the improved level of detail available across the three-dimensional phase space, the power of these results in differentiating models is significantly improved compared to the previous single-differential analysis.

To help visualize some of the notable model differences, the differential cross section over a function of $\cos(\theta_\mu)$ and E_ν, constructed by integrating over P_μ and normalizing by the average neutrino energy $\langle E_\nu \rangle$, is plotted in Fig. 3. The subdivision by neutrino energy helps separate model predictions, which often struggle to describe the data in certain energy slices or between slices. Furthermore, it improves separation between the QE and pion production processes; the QE fraction decreases from ≈75% in the lowest energy bin to ≈55% in the highest energy bin as predicted by `NuWro`, shown in the supplemental material [37]. `GiBUU` yields the best result at describing the data within the lowest two E_ν slices with χ^2/ndf of 36.0/28 and 48.7/35. However, it struggles to describe the correlations between E_ν slices. By comparison `NuWro` gives the best prediction both overall and at the highest neutrino energy, where it has a χ^2/ndf of 28.8/33. There are larger Δ-resonance contributions in this high-E_ν region where notable differences in pion production modeling have been demonstrated [53], especially at low Q^2 and forward lepton angles. A full description of model performances across E_ν slices is found in the supplemental material [37].

Looking forward, this measurement can be enhanced by using the increased statistics of the full BNB dataset, as well as by combining MicroBooNE data from the BNB and the Neutrinos at the Main Injector beamline [54] to further increase the statistics, while reducing the flux-related uncertainties. Furthermore, measurements of the cross section in semi-inclusive and exclusive channels will allow for investigation of the modeling of the hadronic final states.

In summary, we report the nominal-flux-averaged differential inclusive ν_μ CC cross section on argon $d^2\sigma(E_\nu)/d\cos(\theta_\mu)dP_\mu$, using an exposure of 6.4×10^{20} POT of data from the Booster Neutrino Beam at Fermilab. Comparisons with model predictions show the best agreement with `GiBUU` at low energy and with `NuWro` at higher energies, particularly at forward muon scattering angles. However, no model is able to describe the measurement within uncertainties across all energy bins, demonstrating the power of measuring cross sections as a function of neutrino energy. This work advances the field of cross section physics by providing the first measurement over a complete three-dimensional kinematic phase space for inclusive ν_μ CC scattering on argon. This allows for a better understanding of neutrino event generator performance across a broad phase space.

Acknowledgments

This document was prepared by the MicroBooNE collaboration using the resources of the Fermi National Accelerator Laboratory (Fermilab), a U.S. Department of Energy, Office of Science, HEP User Facility. Fermilab is managed by Fermi Research Alliance, LLC (FRA), acting under Contract No. DE-AC02-07CH11359. MicroBooNE is supported by the following: the U.S. Department of Energy, Office of Science, Offices of High Energy Physics and Nuclear Physics; the U.S. National Science Foundation; the Swiss National Science Foundation; the Science and Technology Facilities Council (STFC), part of the United Kingdom Research and Innovation; the Royal Society (United Kingdom); and the UK Research and Innovation (UKRI) Future Leaders Fellowship. Additional support for the laser calibration system and cosmic ray tagger was provided by the Albert Einstein Center for Fundamental Physics, Bern, Switzerland. We also acknowledge the contributions of technical and scientific staff to the design, construction, and operation of the MicroBooNE detector as well as the contributions of past collaborators to the development of MicroBooNE analyses, without whom this work would not have been possible. For the purpose of open access, the authors have applied a Creative Commons Attribution (CC BY) public copyright license to any Author Accepted Manuscript version arising from this submission.

References

[1] NOνA Collaboration, Improved measurement of neutrino oscillation parameters by the NOνA experiment, Phys. Rev. D 106 (2022) 032004. `doi:10.1103/PhysRevD.106.032004`.
URL `https://link.aps.org/doi/10.1103/PhysRevD.106.032004`

[2] T2K Collaboration, Measurements of neutrino oscillation parameters from the T2K experiment using 3.6×10^{21} protons on target, Eur. Phys. J. C 83 (9) (2023) 782. `doi:10.1140/epjc/s10052-023-11819-x`.
URL `https://doi.org/10.1140/epjc/s10052-023-11819-x`

[3] S. Nagu, J. Singh, J. Singh, R. Singh, Impact of cross-sectional uncertainties on DUNE sensitivity due to nuclear effects, Nucl. Phys. B 951 (2020) 114888. `arXiv:1905.13101`, `doi:https://doi.org/10.1016/j.nuclphysb.2019.114888`.
URL `https://www.sciencedirect.com/science/article/pii/S0550321319303748`

[4] L. Alvarez-Ruso, et al., NuSTEC White Paper: Status and challenges of neutrino–nucleus scattering, Prog. Part. Nucl. Phys. 100 (2018) 1–68. `doi:https://doi.org/10.1016/j.ppnp.2018.01.006`.
URL `https://www.sciencedirect.com/science/article/pii/S0146641018300061`

[5] J. A. Formaggio, G. P. Zeller, From eV to EeV: Neutrino cross sections across energy scales, Rev. Mod. Phys. 84 (2012) 1307–1341. `arXiv:1305.7513`, `doi:10.1103/RevModPhys.84.1307`.
URL `https://link.aps.org/doi/10.1103/RevModPhys.84.1307`

[6] DUNE Collaboration, Volume I. Introduction to DUNE, J. Instrum. 15 (08) (2020) T08008–T08008. `doi:10.1088/1748-0221/15/08/t08008`.
URL `https://doi.org/10.1088/1748-0221/15/08/t08008`

[7] MicroBooNE Collaboration, et al., A Proposal for a Three Detector Short-Baseline Neutrino Oscillation Program in the Fermilab Booster Neutrino Beam (2015). `arXiv:1503.01520`.

[8] MicroBooNE Collaboration, First Double-Differential Measurement of Kinematic Imbalance in Neutrino Interactions with the MicroBooNE Detector, Phys. Rev. Lett. 131 (2023) 101802. `doi:10.1103/PhysRevLett.131.101802`.
URL `https://link.aps.org/doi/10.1103/PhysRevLett.131.101802`

[9] MicroBooNE Collaboration, Measurement of neutral current single π^0 production on argon with the MicroBooNE detector, Phys. Rev. D 107 (2023) 012004. `doi:10.1103/PhysRevD.107.012004`.
URL `https://link.aps.org/doi/10.1103/PhysRevD.107.012004`

[10] MINERνA Collaboration, Measurement of inclusive charged-current ν_μ cross sections as a function of muon kinematics at $\langle E_\nu \rangle \sim 6$ GeV on hydrocarbon, Phys. Rev. D 104 (9) (2021) 092007. `arXiv:2106.16210`, `doi:10.1103/PhysRevD.104.092007`.

[11] MINERνA Collaboration, Simultaneous measurement of muon neutrino ν_μ charged-current single π^+ production in CH, C, H_2O, Fe, and Pb targets in MINERνA (9 2022). `arXiv:2209.07852`.

[12] T2K Collaboration, Simultaneous measurement of the muon neutrino charged-current cross section on oxygen and carbon without pions in the final state at T2K, Phys. Rev. D 101 (11) (2020) 112004. `arXiv:2004.05434`, `doi:10.1103/PhysRevD.101.112004`.

[13] T2K Collaboration, Measurements of $\overline{\nu}_\mu$ and $\overline{\nu}_\mu + \nu_\mu$ charged-current cross-sections without detected pions or protons on water and hydrocarbon at a mean anti-neutrino energy of 0.86 GeV, PTEP 2021 (4) (2021) 043C01. `arXiv:2004.13989`, `doi:10.1093/ptep/ptab014`.

[14] MINERνA Collaboration, Simultaneous Measurement of Proton and Lepton Kinematics in Quasielasticlike ν_μ-Hydrocarbon Interactions from 2 to 20 GeV, Phys. Rev. Lett. 129 (2) (2022) 021803. `arXiv:2203.08022`, `doi:10.1103/PhysRevLett.129.021803`.

[15] ArgoNeuT Collaboration, First measurements of inclusive muon neutrino charged current differential cross sections on argon, Phys. Rev. Lett. 108 (2012) 161802. `arXiv:1111.0103`, `doi:10.1103/PhysRevLett.108.161802`.
URL `https://link.aps.org/doi/10.1103/PhysRevLett.108.161802`

[16] ArgoNeuT Collaboration, Measurements of inclusive muon neutrino and antineutrino charged current differential cross sections on argon in the NuMI antineutrino beam, Phys. Rev. D 89 (2014) 112003. `arXiv:1404.4809`, `doi:10.1103/PhysRevD.89.112003`.
URL `https://link.aps.org/doi/10.1103/PhysRevD.89.112003`

[17] MicroBooNE Collaboration, First measurement of inclusive muon neutrino charged current differential cross sections on argon at $E_\nu \sim 0.8$ GeV with the MicroBooNE detector, Phys. Rev. Lett. 123 (2019) 131801. `arXiv:1905.09694`, `doi:10.1103/PhysRevLett.123.131801`.
URL `https://link.aps.org/doi/10.1103/PhysRevLett.123.131801`

[18] MicroBooNE Collaboration, First measurement of energy-dependent inclusive muon neutrino charged-current cross sections on argon with the MicroBooNE detector, Phys. Rev. Lett. 128 (2022) 151801. `arXiv:2110.14023`, `doi:10.1103/PhysRevLett.128.151801`.
URL `https://link.aps.org/doi/10.1103/PhysRevLett.128.151801`

[19] MicroBooNE Collaboration, Search for an anomalous excess of inclusive charged-current ν_e interactions in the MicroBooNE experiment using Wire-Cell reconstruction, Phys. Rev. D 105 (2022) 112005. `arXiv:2110.13978`, `doi:10.1103/PhysRevD.105.112005`.
URL `https://link.aps.org/doi/10.1103/PhysRevD.105.112005`

[20] MicroBooNE Collaboration, Design and construction of the MicroBooNE detector, J. Instrum. 12 (02) (2017) P02017. `arXiv:1612.05824`, `doi:10.1088/1748-0221/12/02/P02017`.
URL `https://dx.doi.org/10.1088/1748-0221/12/02/P02017`

[21] MiniBooNE Collaboration, The Neutrino Flux prediction at MiniBooNE, Phys. Rev. D 79 (2009) 072002. `arXiv:0806.1449`, `doi:10.1103/PhysRevD.79.072002`.

[22] X. Qian, C. Zhang, B. Viren, M. Diwan, Three-dimensional Imaging for Large LArTPCs, J. Instrum. 13 (05) (2018) P05032. `arXiv:1803.04850`, `doi:10.1088/1748-0221/13/05/P05032`.

[23] MicroBooNE Collaboration, Cosmic Ray Background Rejection with Wire-Cell LArTPC Event Reconstruction

in the MicroBooNE Detector, Phys. Rev. Applied 15 (6) (2021) 064071. `arXiv:2101.05076`, `doi:10.1103/PhysRevApplied.15.064071`.

[24] MicroBooNE Collaboration, Wire-cell 3D pattern recognition techniques for neutrino event reconstruction in large LArTPCs: algorithm description and quantitative evaluation with MicroBooNE simulation, J. Instrum. 17 (01) (2022) P01037. `arXiv:2110.13961`, `doi:10.1088/1748-0221/17/01/p01037`.
URL `https://doi.org/10.1088%2F1748-0221%2F17%2F01%2Fp01037`

[25] T. Chen, C. Guestrin, XGBoost: A Scalable Tree Boosting System, 2016. `arXiv:1603.02754`, `doi:10.1145/2939672.2939785`.

[26] PSTAR at NIST: `https://physics.nist.gov/PhysRefData/Star/Text/PSTAR.html`.

[27] MicroBooNE Collaboration, Calibration of the Charge and Energy Response of the MicroBooNE Liquid Argon Time Projection Chamber using Muons and Protons, J. Instrum. 15 (03) (2020) P03022. `arXiv:1907.11736`, `doi:10.1088/1748-0221/15/03/P03022`.

[28] MicroBooNE Collaboration, Neutrino event selection in the MicroBooNE liquid argon time projection chamber using Wire-Cell 3D imaging, clustering, and charge-light matching, J. Instrum. 16 (06) (2021) P06043. `arXiv:2011.01375`, `doi:10.1088/1748-0221/16/06/P06043`.

[29] MicroBooNE Collaboration, Reconstruction and Measurement of $\mathcal{O}(100)$ MeV Energy Electromagnetic Activity from $\pi^0 \to \gamma\gamma$ Decays in the MicroBooNE LArTPC, J. Instrum. 15 (02) (2020) P02007. `arXiv:1910.02166`, `doi:10.1088/1748-0221/15/02/p02007`.

[30] S. Sukhoruchkin, Z. Soroko, Atomic Mass and Nuclear Binding Energy for Ar-40 (Argon), Springer-Verlag Berlin Heidelberg, 2009. `doi:10.1007/978-3-540-69945-3_558`.
URL `https://materials.springer.com/lb/docs/sm_lbs_978-3-540-69945-3_558`

[31] MicroBooNE Collaboration, New CC0π GENIE model tune for MicroBooNE, Phys. Rev. D 105 (2022) 072001. `arXiv:2110.14028`, `doi:10.1103/PhysRevD.105.072001`.
URL `https://link.aps.org/doi/10.1103/PhysRevD.105.072001`

[32] T2K Collaboration, Measurement of double-differential muon neutrino charged-current interactions on C_8H_8 without pions in the final state using the T2K off-axis beam, Phys. Rev. D 93 (11) (2016) 112012. `arXiv:1602.03652`, `doi:10.1103/PhysRevD.93.112012`.

[33] GENIE Collaboration, The GENIE Neutrino Monte Carlo Generator: Physics and User Manual (2015). `arXiv:1510.05494`.

[34] S. Agostinelli, et al., Geant4—a simulation toolkit, Nucl. Instrum. Meth. A 506 (3) (2003) 250–303. `doi:https://doi.org/10.1016/S0168-9002(03)01368-8`.
URL `https://www.sciencedirect.com/science/article/pii/S0168900203013688`

[35] B. P. Roe, Statistical errors in Monte Carlo estimates of systematic errors, Nucl. Instrum. Meth. A 570 (2006) 159–164. `doi:https://doi.org/10.1016/j.nima.2006.10.009`.
URL `https://www.sciencedirect.com/science/article/abs/pii/S0168900206018055?via%3Dihub`

[36] C. A. Argüelles, A. Schneider, T. Yuan, A binned likelihood for stochastic models, J. High Energy Phys. 06 (2019) 030. `arXiv:1901.04645`, `doi:10.1007/JHEP06(2019)030`.

[37] See Supplemental Material at for treatment of detector systematic uncertainties, validation of overall model, master equation of unfolding, and tabulated values of cross section and covariance matrices. (2024).

[38] MicroBooNE Collaboration, Novel approach for evaluating detector-related uncertainties in a LArTPC using MicroBooNE data, Eur. Phys. J. C 82 (2022) 454. `arXiv:2111.03556`, `doi:https://doi.org/10.1140/epjc/s10052-022-10270-8`.

[39] MicroBooNE Collaboration, Measurement of space charge effects in the MicroBooNE LArTPC using cosmic muons, J. Instrum. 15 (12) (2020) P12037. `arXiv:2008.09765`, `doi:10.1088/1748-0221/15/12/P12037`.

[40] MicroBooNE Collaboration, A Method to Determine the Electric Field of Liquid Argon Time Projection Chambers Using a UV Laser System and its Application in MicroBooNE, J. Instrum. 15 (07) (2020) P07010. `arXiv:1910.01430`, `doi:10.1088/1748-0221/15/07/P07010`.

[41] C. E. Rasmussen, C. K. I. Williams, Gaussian Processes for Machine Learning (Adaptive Computation and Machine Learning), The MIT Press, 2005.

[42] M. Frate, K. Cranmer, S. Kalia, A. Vandenberg-Rodes, D. Whiteson, Modeling smooth backgrounds and generic localized signals with gaussian processes (2017). `arXiv:1709.05681`.

[43] L. Li, N. Nayak, J. Bian, P. Baldi, Efficient neutrino oscillation parameter inference using gaussian processes, Phys. Rev. D 101 (2020) 012001. `arXiv:1811.07050v2`, `doi:10.1103/PhysRevD.101.012001`.
URL `https://link.aps.org/doi/10.1103/PhysRevD.101.012001`

[44] M. L. Eaton, Multivariate Statistics: a Vector Space Approach, John Wiley and Sons Inc, 1983.

[45] W. Tang, X. Li, X. Qian, H. Wei, C. Zhang, Data Unfolding with Wiener-SVD Method, J. Instrum. 12 (10) (2017) P10002. `arXiv:1705.03568`, `doi:10.1088/1748-0221/12/10/P10002`.

[46] X. Ji, W. Gu, X. Qian, H. Wei, C. Zhang, Combined Neyman–Pearson chi-square: An improved approximation

to the Poisson-likelihood chi-square, Nucl. Instrum. Meth. A 961 (2020) 163677. `arXiv:1903.07185`, `doi:10.1016/j.nima.2020.163677`.

[47] T. Golan, J. T. Sobczyk, J. Zmuda, NuWro: the Wroclaw Monte Carlo Generator of Neutrino Interactions, Nucl. Phys. B Proc. Suppl. 229-232 (2012) 499–499. `doi:10.1016/j.nuclphysbps.2012.09.136`.

[48] GENIE Collaboration, The GENIE Neutrino Monte Carlo Generator, Nucl. Instrum. Meth. A 614 (2010) 87–104. `arXiv:0905.2517`, `doi:10.1016/j.nima.2009.12.009`.

[49] GENIE Collaboration, Recent highlights from GENIE v3, Eur. Phys. J. S. T. 230 (24) (2021) 4449–4467. `arXiv:2106.09381`, `doi:10.1140/epjs/s11734-021-00295-7`.
URL `https://doi.org/10.1140/epjs/s11734-021-00295-7`

[50] O. Buss, T. Gaitanos, K. Gallmeister, H. van Hees, M. Kaskulov, O. Lalakulich, A. B. Larionov, T. Leitner, J. Weil, U. Mosel, Transport-theoretical Description of Nuclear Reactions, Phys. Rept. 512 (2012) 1–124. `arXiv:1106.1344`, `doi:10.1016/j.physrep.2011.12.001`.

[51] Y. Hayato, A neutrino interaction simulation program library NEUT, Acta Phys. Polon. B 40 (2009) 2477–2489.

[52] M. B. Avanzini, et al., Comparisons and challenges of modern neutrino-scattering experiments, Phys. Rev. D 105 (9) (2022) 092004. `arXiv:2112.09194`, `doi:10.1103/PhysRevD.105.092004`.

[53] MINERνA Collaboration, Tuning the GENIE pion production model with MINERνA data, Phys. Rev. D 100 (2019) 072005. `arXiv:1903.01558`, `doi:10.1103/PhysRevD.100.072005`.
URL `https://link.aps.org/doi/10.1103/PhysRevD.100.072005`

[54] MINERνA Collaboration, Neutrino flux predictions for the NuMI beam, Phys. Rev. D 94 (2016) 092005. `arXiv:1607.00704`, `doi:10.1103/PhysRevD.94.092005`.
URL `https://link.aps.org/doi/10.1103/PhysRevD.94.092005`

Supplemental Materials: Measurement of three-dimensional inclusive muon-neutrino charged-current cross sections on argon with the MicroBooNE detector

August 30, 2024

I. SMOOTHING OF DETECTOR SYSTEMATIC UNCERTAINTIES

This section provides a detailed description of how the Gaussian Processes Regression (GPR) smoothing algorithm [1–3] is used to reduce the overestimation of detector systematic uncertainties that result from a limited quantity of Monte Carlo (MC) simulation available. A bootstrapping procedure, discussed extensively in Ref. [4] and briefly reviewed here, is used to estimate the uncertainty in the detector response.

This process involves comparing the distribution of events simulated using nominal detector response parameter values to the distribution of events simulated using detector response parameter values under offsets constructed by observing the difference between data and nominal MC prediction [5]. The dataset used in this comparison consists of cosmic rays that cross either the anode or cathode plane to enable accurate reconstruction. These offsets are treated as 1σ variations, and each pair of distributions, under nominal and offset detector response parameter values, is referred to as one "universe". The difference between the nominal and 1σ distributions is referred to as $\vec{V}_D$, and the average difference over all universes is referred to as $\vec{V}_D^{\text{nominal}}$. A covariance matrix M_R is computed from the set of all difference vectors $\vec{V}_D$ to represent the uncertainty in estimating $\vec{V}_D^{\text{nominal}}$. Since there is a limited quantity of simulation available, there are statistical fluctuations present in the set of $\vec{V}_D$, and therefore in the computation of M_R. This problem is amplified in multiple dimensions, where the large number of bins further restricts the number of events per bin. The smoothing procedure aims to address the large statistical fluctuations present by describing the set of $\vec{V}_D$ and corresponding M_R with a smooth distribution.

In general, GPR aims to produce a smoothed prediction over a target set of points, $\vec{x}_a$, by incorporating information from measurements, $\vec{y}_b$, at positions $\vec{x}_b$. Note that the subscripts a and b are used to identify the distribution being referenced, while i and j, shown later, are used to identify a particular bin within a distribution. GPR begins with an uninformed prior of a joint normal distribution with a zero mean vector and an identity covariance matrix, $p(\vec{x}) = N_{\vec{x}}(\vec{0}, I)$, on the target distribution as well as the measured distribution. The measurement $\vec{y}_b$ and corresponding covariance Σ_y are used in combination with a kernel matrix Σ_K to generate an updated posterior prediction $p(\vec{x}_a|\vec{x}_b)$ with mean $\vec{\mu}_{a|b}$ and covariance $\Sigma_{T,a|b}$. The kernel matrix describes the level of correlation between any two bins, and is computed using a kernel function $K(\vec{x}_i, \vec{x}_j)$. By choosing a function that decays with distance, the physical intuition of smoothness can be applied by treating nearby bins as highly correlated. The kernel matrix is added to the measured covariance to form a total covariance Σ_T:

$$\Sigma_{K;ij} = K(\vec{x}_i, \vec{x}_j), \tag{1}$$

$$\Sigma_T = \Sigma_y + \Sigma_K. \tag{2}$$

From these, Bayes' theorem is used to compute the posterior distribution:

$$p(\vec{x}_a|\vec{x}_b) = N_{x_a}(\vec{\mu}_{a|b}, \Sigma_{T,a|b}) \tag{3}$$

where the mean and covariance are computed using:

$$\vec{\mu}_{a|b} = \vec{\mu}_a + \Sigma_{K,ab}\Sigma_{T,bb}^{-1}(\vec{y}_b - \vec{\mu}_b), \tag{4}$$

$$\Sigma_{T,a|b} = \Sigma_{K,aa} - \Sigma_{K,ab}\Sigma_{T,bb}^{-1}\Sigma_{K,ba}. \tag{5}$$

Here $\vec{\mu}_a$ and $\vec{\mu}_b$ are the prior means at points $\vec{x}_a$ and $\vec{x}_b$, respectively.

From Eq. (4), we can see that the difference between measured and predicted values, $\vec{y}_b - \vec{\mu}_b$, is used to update the mean prediction. However, measurements with large uncertainty will contribute less to the posterior distribution, as the term $\Sigma_{T,bb}^{-1}$ will be suppressed. This mathematical framework used to compute the posterior distribution is identical to that in Sec. II in the conditional constraint formalism. This work computes the posterior prediction over the target distribution at the same bin centers as used in the measured distribution $\vec{y}_b = \vec{V}_D^{\text{nominal}}$, i.e $\vec{x}_a = \vec{x}_b$.

However, in principle the GPR technique can be used to obtain predictions using any set of points, not just at $\vec{x}_b$. The kernel function is computed using a radial basis function (RBF), which asserts the intuition of smoothness by assigning a correlation that decays exponentially as the distance squared between bin centers increases:

$$K(\vec{x}_i, \vec{x}_j) = e^{-|(\vec{x}_i - \vec{x}_j)\cdot\vec{s}|^2/2}, \tag{6}$$

$$s_k = \frac{1}{L_k}. \tag{7}$$

The bin centers $\vec{x}_i$ and $\vec{x}_j$ are three-dimensional vectors describing their location within the kinematic phase space. Here, L_k denotes a characteristic length scale for each dimension over which the points are sufficiently correlated. The RBF kernel considers very close points to be highly correlated, and is strictly decreasing as a function of distance between points as it exponentially decays towards zero, treating distant points as almost fully uncorrelated. This causes nearby points to play a significant role in shaping the posterior prediction at a given location, while distant points have almost no effect, as can be seen in Eq. (4), where Σ_K acts on the measurement $(\vec{y}_b - \vec{\mu}_b)$.

In the reported work, the RBF kernel utilizes three characteristic length scales for the neutrino energy, muon momentum, and muon forward angle axes. Based on the measured kinematic resolutions, length scales were chosen to be 0.1 in $\cos(\theta_\mu^{\mathrm{rec}})$ and relative 20% for each of E_ν^{rec} and P_μ^{rec}, the latter achieved by using a length scale of $\ln(1.2)$ and natural log values of E_ν^{rec} and P_μ^{rec} in $\vec{x}_i$ and $\vec{x}_j$ in Eq. (6). Given the length scales and measured data, Eq. (4) and Eq. (5) therefore directly give us the mean and covariance of the smoothed posterior prediction. These become the new values for $\vec{V}_D^{\mathrm{nominal}}$ and M_R, and consequently reduce the detector uncertainty by a factor of twenty from ≈400% to ≈20%, reducing the overestimation of uncertainties from finite MC simulation statistics. The detector response uncertainties computed with the use of smoothing in this three-dimensional measurement were compared to counterparts on single-differential measurements [6], where statistical fluctuations are small and smoothing was not used. In all cases, the detector response uncertainties in this three-dimensional analysis were found to be comparable or larger than those counterparts, demonstrating that smoothing has not suppressed the uncertainty estimation beyond what is achieved in a high statistics scenario. The impact of smoothing can be seen in Fig. 1, which also shows the breakdown of uncertainties from each source over the 138 analysis bins in true space. To help understand the overall magnitude of uncertainties across the truth phase space, Fig. 2 presents the total fractional uncertainty in each analysis bin. Even after using GPR smoothing, detector response uncertainties are still the second largest source of uncertainties in the analysis behind statistical uncertainties.

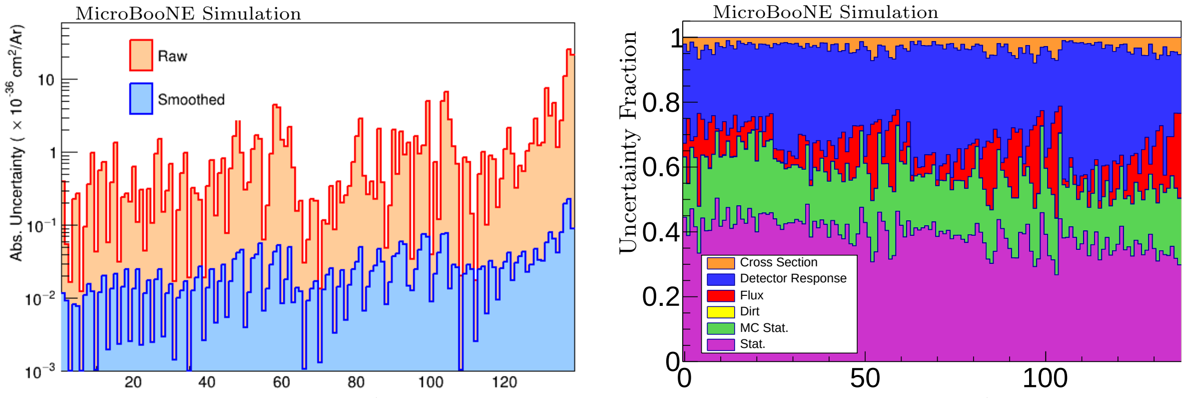

FIG. 1. a) Comparison of the detector response diagonal uncertainties in the cases with and without the use of GPR smoothing, demonstrating an order of magnitude reduction in detector response uncertainty estimation. b) Breakdown of total uncertainties across the various statistical and systematic sources, including the use of GPR smoothing in the estimation of the detector response uncertainty, plotted as a fraction of the total diagonal uncertainty in each bin.

II. VALIDATION OF OVERALL MODEL

To ensure that the unfolded cross sections are not biased beyond the estimated uncertainties, it is important to demonstrate that the MicroBooNE model prediction and uncertainties cover the distribution seen in data. This

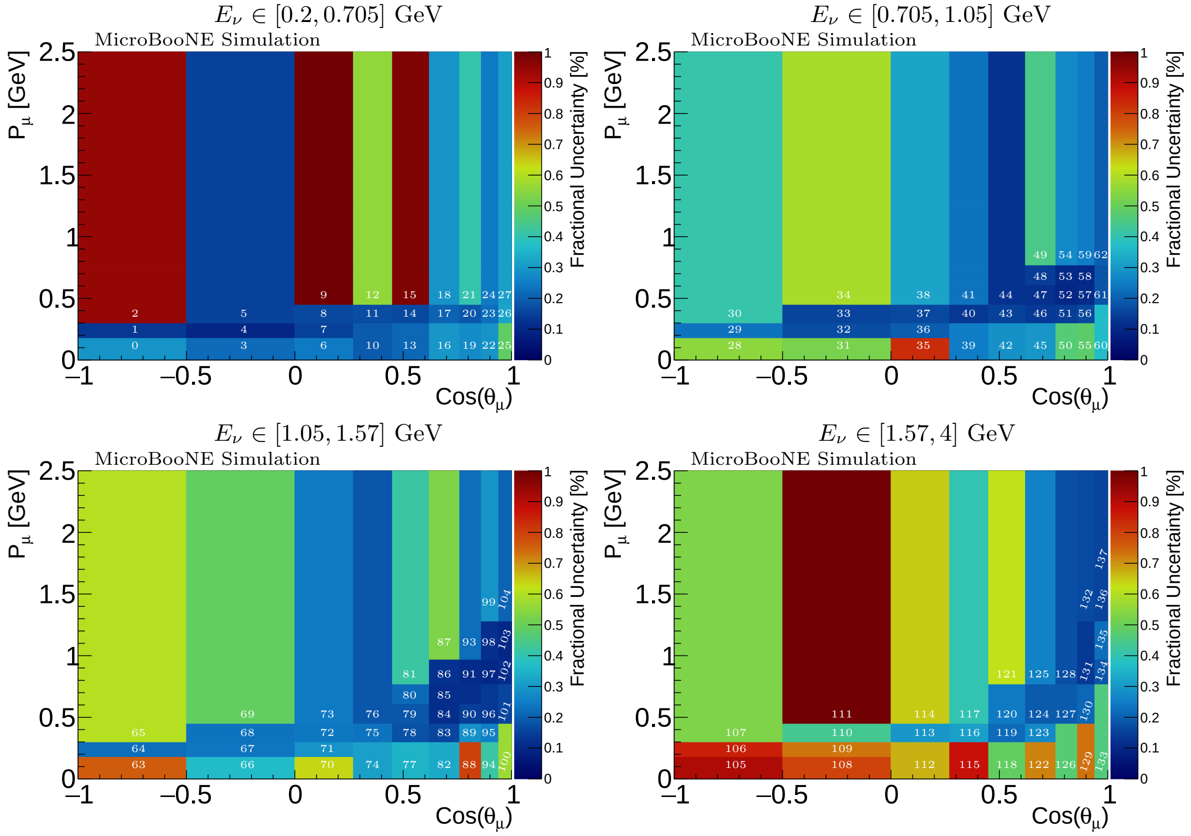

FIG. 2. Total uncertainty as a fraction of the predicted cross section from the MicroBooNE model in the corresponding bin. The four sub-figures each present a different E_ν slice. The total uncertainty comes from the square root of the covariance matrix diagonal entries. Analysis bin number overlaid on top of each bin near the bottom.

ensures that the MicroBooNE model is a reliable estimate of the response matrix used in unfolding. We use a validation procedure to evaluate the signal and background model prediction (P)'s capability to describe the data measurement (M) within P's uncertainty through a χ^2 goodness-of-fit (GoF) test, based on the test statistic:

$$\chi^2 = (M - P)^T \times C_{\text{full}}^{-1}(M, P) \times (M - P)\,, \tag{8}$$

where the covariance matrix C_{full}^{-1} is the full covariance matrix including both statistical and systematic uncertainties. To validate the model across the full three-dimensional phase space $\{E_\nu, P_\mu, \cos(\theta_\mu)\}$, it is important to maintain a nonzero efficiency. The selection efficiency across the phase space is shown in Fig. 3. For a given bin in truth variables, the selection efficiency is computed as the ratio of selected to total events with truth kinematics corresponding to that bin.

The GoF test evaluates the null hypothesis that the overall model prediction, including uncertainties, is able to cover the distribution seen in data. Note that here by model we refer to the central value along with its uncertainties. This evaluation can be narrowed to a specific portion of modeling by using the conditional covariance matrix formalism [7], which uses Bayes' theorem similar to how it is used in Sec. I. Let μ and Σ represent the central value and covariance predicted by the model over two channels U and V, with corresponding data measurement n:

$$\Sigma = \begin{pmatrix} \Sigma^{UU} & \Sigma^{UV} \\ \Sigma^{VU} & \Sigma^{VV} \end{pmatrix}. \tag{9}$$

For example, the U channel could represent the distribution of events over $E_{\text{had}}^{\text{rec}}$, while the V channel could represent the distribution of events over P_μ^{rec}. Then we can derive the posterior prediction on U given the constraints on V:

$$\begin{aligned} \mu^{U,\text{constrained}} &= \mu^U + \Sigma^{UV} \times \left(\Sigma^{VV}\right)^{-1} \times \left(n^V - \mu^V\right), \\ \Sigma^{UU,\text{constrained}} &= \Sigma^{UU} - \Sigma^{UV} \times \left(\Sigma^{VV}\right)^{-1} \times \Sigma^{VU}. \end{aligned} \tag{10}$$

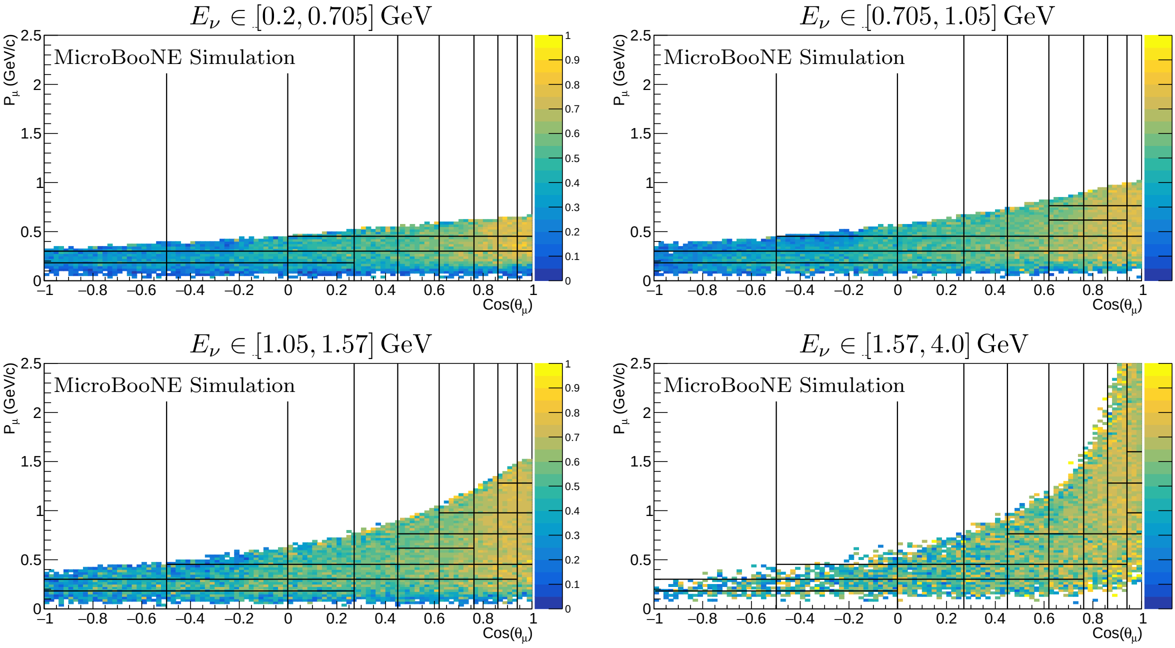

FIG. 3. Selection efficiency for simulated events over $\{P_\mu, \cos(\theta_\mu)\}$ within each E_ν slice. Bin edges are indicated by black lines. Bins containing under 5 events in truth are not drawn because of their low statistics.

Following the example distributions chosen above, the muon momentum measurement would be used as a constraint on the hadronic energy prediction, updating the model prediction on hadronic energy to exclude regions in disagreement with the measurement over muon momentum. A GoF test can be performed on V first, and then performed on U while using the data distribution on V as a constraint. This allows for examination of the modeling of the correlated predictions over U and V.

In particular, this allows us to evaluate the GoF of the distribution over $\{E^{\rm rec}_{\rm had}, \cos(\theta^{\rm rec}_\mu)\}$ using $\{P^{\rm rec}_\mu, \cos(\theta^{\rm rec}_\mu)\}$ as a constraint. Note that since the inclusive ν_μ CC channel is described by three degrees of freedom, it is not possible to form independent three-dimensional channels U and V, and so no three-dimensional constrained GoF test can be performed. Therefore, the two-dimensional channels used provide the best test of the kinematic phase space. There are key features of the conditional constraint procedure and corresponding validation tests over distributions of hadronic energy that are worth mentioning in detail. First, the posterior model prediction on U given the constraint on V will have greatly reduced uncertainties. This is because the model predictions and their uncertainties over various kinematic distributions are correlated, so that restricting the allowed phase space of model parameters to fit the data on V also constrains the model prediction on U. As a result, the common systematic uncertainties between U and V are greatly reduced for the posterior prediction on V.

This results in a validation test that is more sensitive to mismodeling than the overall unfolded measurement, which uses the default MicroBooNE model without application of the conditional constraint procedure during the unfolding. For example, large correlated neutrino flux uncertainties can hide issues in the modeling of missing hadronic energy. A basic GoF test may not detect this mismodeling, but the unfolded measurement may still be affected. However, through the conditional covariance formalism, correlated neutrino flux uncertainties between the muon kinematics and hadronic energy are removed, allowing the mismodeling to be detected by the constrained GoF test. This fact is demonstrated through fake data studies in section III, where model validation tests on fake data are able to detect significant mismodeling before the bias introduced is larger than the uncertainties on the unfolded measurement.

In the case of the model validation of the hadronic energy prediction, the use of the muon kinematics measurement as a constraint allows for validation of the correlations between the muon kinematics and hadronic energy modeling. This is particularly important because it creates a GoF test on the constrained model prediction over the $\{E^{\rm rec}_{\rm had}, \cos(\theta^{\rm rec}_\mu)\}$ distribution that is sensitive to the modeling of missing energy, allowing for the mapping from energy transfer ν to $E^{\rm rec}_{\rm had}$ to be validated. This point can be seen intuitively in two ways.

First, through conservation of energy the sensitivity to the modeling of $E^{\rm missing}_{\rm had}$ can be seen:

$$E_\nu = E_\mu + E^{\rm rec}_{\rm had} + E^{\rm missing}_{\rm had}. \tag{11}$$

$E^{\rm rec}_{\rm had}$ is directly measured, E_μ is determined through the measurement of $P^{\rm rec}_\mu$, and the distribution over E_ν is controlled by the flux prediction, which is constrained by the muon kinematics measurements. This leaves $E_{\mathrm{had}}^{\mathrm{missing}}$ as the only undetermined quantity, meaning that the constrained GoF test is sensitive to its mismodeling.

Second, the model predictions over $E_{\mathrm{had}}^{\mathrm{missing}}$, $E_{\mathrm{had}}^{\mathrm{rec}}$, and P_{μ}^{rec} are correlated as a result of simulating the underlying neutrino interaction channels such as quasi-elastic (QE), resonance (RES), and deep inelastic scattering (DIS). Additionally, the $\{P_{\mu}^{\mathrm{rec}}, \cos(\theta_{\mu}^{\mathrm{rec}})\}$ measurement constrains the space of model variations across the interaction channels, creating an effect similar to re-weighting the hadronic system using the muon kinematics as a sideband. Furthermore, the model predictions over interaction channels each vary as a function of the muon scattering angle $\theta_{\mu}^{\mathrm{rec}}$, forming detailed sets of predictions in two dimensions. This allows the constrained GoF test in two dimensions to perform a detailed examination of the model performance, going beyond the level of validation possible in one dimension. As a result, the constrained GoF test over $\{E_{\mathrm{had}}^{\mathrm{rec}}, \cos(\theta_{\mu}^{\mathrm{rec}})\}$ tests the modeling of correlations between the kinematic distributions, making it sensitive to the modeling of $E_{\mathrm{had}}^{\mathrm{missing}}$.

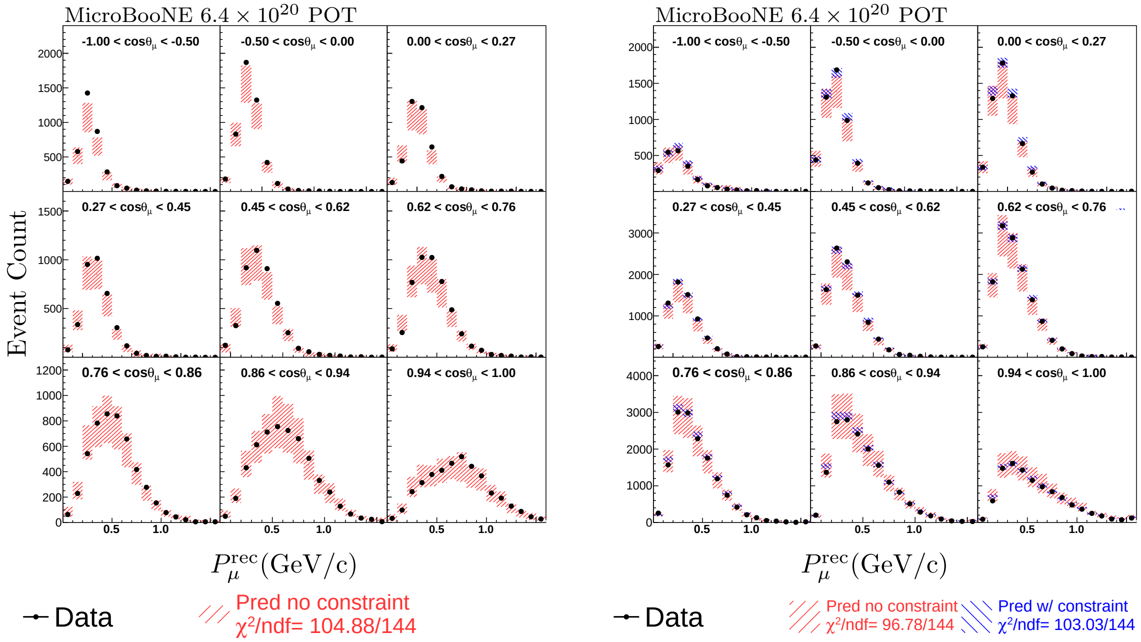

(a) (b)

FIG. 4. Comparison between data and prediction over the muon kinematic distribution $\{P_{\mu}^{\mathrm{rec}}, \cos(\theta_{\mu}^{\mathrm{rec}})\}$ for fully contained events in (a) and partially contained events in (b). The fully contained distribution is used as a constraint on the model prediction for the partially constrained distribution following Eq. 10. The statistical and systematic uncertainties of the data and simulation are included in the uncertainty bands shown with the model prediction.

Figure 4 demonstrates model validation over the muon kinematic distribution $\{P_{\mu}^{\mathrm{rec}}, \cos(\theta_{\mu}^{\mathrm{rec}})\}$, and Fig. 5 demonstrates model validation over $\{E_{\mathrm{had}}^{\mathrm{rec}}, \cos(\theta_{\mu}^{\mathrm{rec}})\}$. In all cases, the model validation tests find that the model prediction contains enough uncertainties to describe the distribution seen in data, with χ^2/ndf values less than 1. If any corresponding p-values are outside 2σ, the `MicroBooNE model` is determined to fail model validation, requiring the model to be sufficienctly expanded before proceeding with unfolding. By contrast, since the `MicroBooNE model` passed all model validation tests, it can confidently be used in unfolding.

III. FAKE DATA STUDIES

Fake data studies are used to verify the sensitivity of the data-driven model validation. In the previous analysis [8], fake data studies were performed on single-dimensional distributions. In this analysis, additional fake data studies are performed featuring an unfolding to the three-dimensional analysis binning. For each fake data study, we examine whether the `MicroBooNE model` is able to describe the distribution of fully contained events, partially contained events, and the joint distribution of fully contained and partially contained events. For a fake data study to pass validation, the p-value for an associated GoF test must be more extreme than the p-value of the corresponding extracted cross section, demonstrating that we are able to detect the mismodeling at a higher significance than is found in the unfolded measurement. This ensures that if such a mismodeling were present in the data to a degree that would significantly bias the unfolded measurement, we would have previously detected it in the model validation

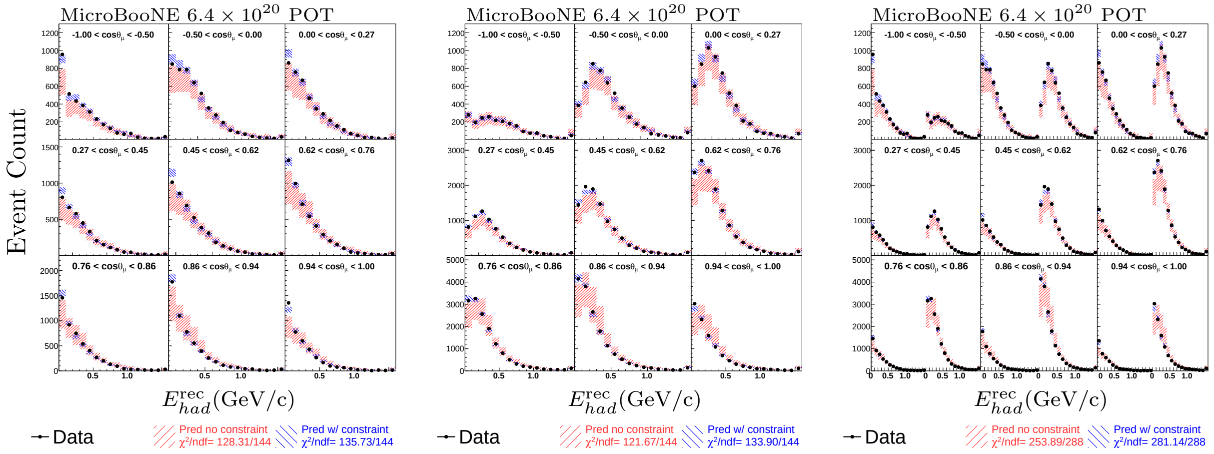

(a) (b) (c)

FIG. 5. Comparison between data and prediction over the 2D distribution $\{E_{\rm had}^{\rm rec}, \cos(\theta_\mu^{\rm rec})\}$ for (a) fully contained events, (b) partially contained events, and (c) both, with the fully contained distribution to the left of the partially contained distribution within each subplot. The red (blue) band gives the uncertainty before (after) applying the 2D $\{P_\mu^{\rm rec}, \cos(\theta_\mu^{\rm rec})\}$ distribution as a constraint on the model prediction following Eq. 10. The statistical and systematic uncertainties of the data and simulation are included in the uncertainty bands shown with the model prediction.

tests.

Because these fake data studies only feature differences in cross section modeling (and event generation in the case of NuWro), we compliment the suite of tests performed using all uncertainties, which parallel those in the previous section, with a parallel series of tests that only use cross section and statistical uncertainties. This provides the strictest criteria for a fake data study to pass model validation, as each distribution is evaluated both under the narrow set of uncertainties that pertain to the variations induced, as well as the full set of uncertainties that provide a direct counterpart to the model validation tests on data. Since model validation is only considered to pass if all tests pass, the presentation of distributions is limited to only those demonstrating the largest mismodeling for each fake data study.

The `NuWro 19.02.01` model provides an independent alternative cross section prediction to the one provided by GENIE v3.0.6 in the `MicroBooNE model`. To test this prediction, a `NuWro` dataset corresponding to 6.1 × 10^{20} POT of data is simulated and used in a fake data study. Model validation tests are performed on the joint distribution of partially and fully contained events, shown in Fig. 6, and the distribution of partially contained events, shown in Fig. 7, both including a version containing all uncertainties and a version containing only cross section and statistical uncertainties. The model performance is observed over the $\{E_{\rm had}, \cos(\theta_\mu)\}$ distribution before and after applying the fake data $\{P_\mu, \cos(\theta_\mu)\}$ distribution as a constraint.

With only cross section and statistical uncertainties, the constrained model validation test detects the mismodeling with a χ^2/ndf of 375.51/288 and corresponding p-value of 0.0004. If this level of disagreement (above 2σ) were found in real data, the model would have to be expanded before confidently being used in unfolding. An example of this procedure in practice can be found in [9] that investigated in detail the hadronic final state. In the case of this `NuWro` fake data study, unfolding is still performed to investigate the degree of bias introduced, which yields a χ^2/ndf of 147.9/138 and corresponding p-value of 0.267 when compared to the statistically independent `NuWro` model truth prediction. This demonstrates the improved sensitivity of the constrained GoF test, which detects the mismodeling beyond 3σ, while the unfolded measurement remains well under 2σ. Using all model uncertainties, GoF tests do not detect mismodeling and yield a χ^2/ndf of 125.18/144 and corresponding p-value of 0.87, and the bias in the unfolded measurement is within uncertainties with a χ^2/ndf of 95.4/138 and corresponding p-value of 0.998.

One potential source of mismodeling is the distribution of energy transfer into its visible and missing components. To examine the impact of mismodeling in this mapping on the unfolded measurement, a series of fake data studies are performed by varying the reconstructed proton energy on a per-event basis. This is conducted in 5% increments, from 70% scaling, representing an excess of missing energy, to 130% scaling, representing a deficit of missing energy compared to the `MicroBooNE model` prediction. Like with the `NuWro` fake data study, GoF tests and unfolded cross sections are computed both using the full uncertainties in the model and using only cross section and statistical uncertainties.

The mismodeling detected in GoF tests, performed on the partially contained $\{E_{\rm had}, \cos(\theta_\mu)\}$ distribution under constraint by the $\{P_\mu, \cos(\theta_\mu)\}$ distribution, as well as the bias in the extracted cross section, can be found in Table I.

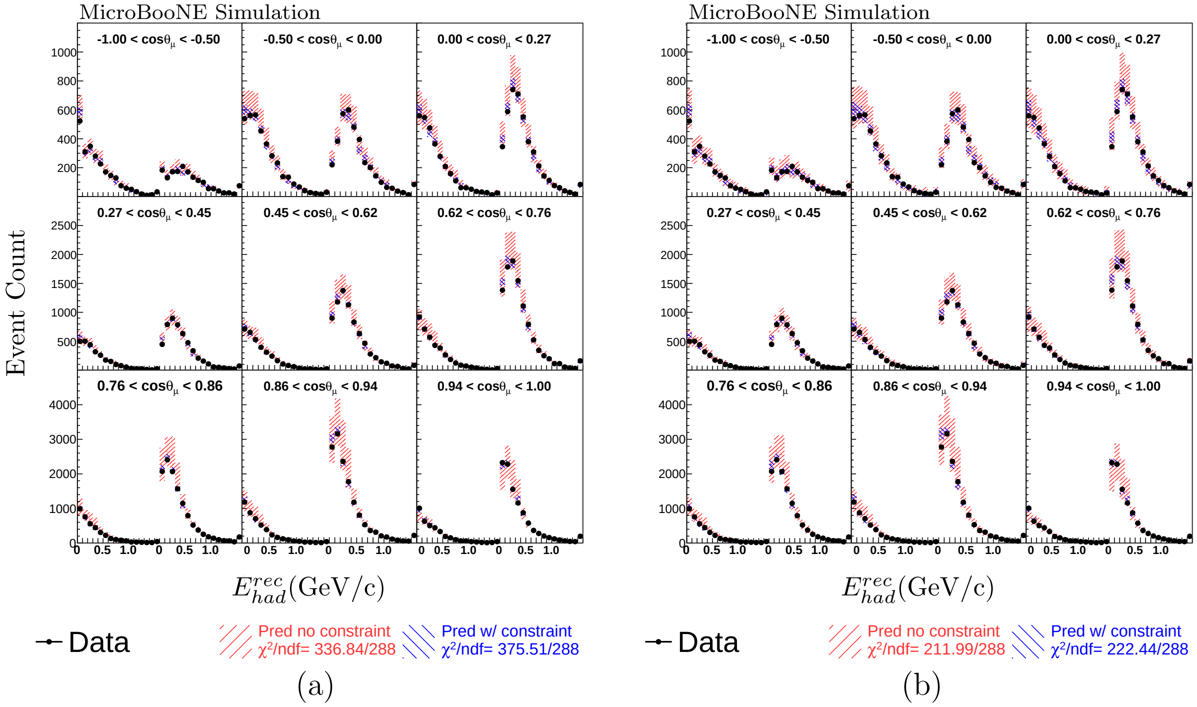

FIG. 6. Comparison of the joint distribution of partially contained and partially contained events between `NuWro` fake data and model and prediction using (a) cross section and statistical uncertainties and (b) all uncertainties over the 2D distribution $\{E^{\rm rec}_{\rm had}, \cos(\theta^{\rm rec}_{\mu})\}$. Within each angle slice, the fully contained event distribution is shown on the left and the partially contained event distribution is shown on the right. The red (blue) band gives the uncertainty before (after) applying the 2D $\{P^{\rm rec}_{\mu}, \cos(\theta^{\rm rec}_{\mu})\}$ distribution as a constraint on the model prediction following Eq. 10. The statistical and systematic uncertainties of the data and simulation are included in the uncertainty bands shown with the model prediction.

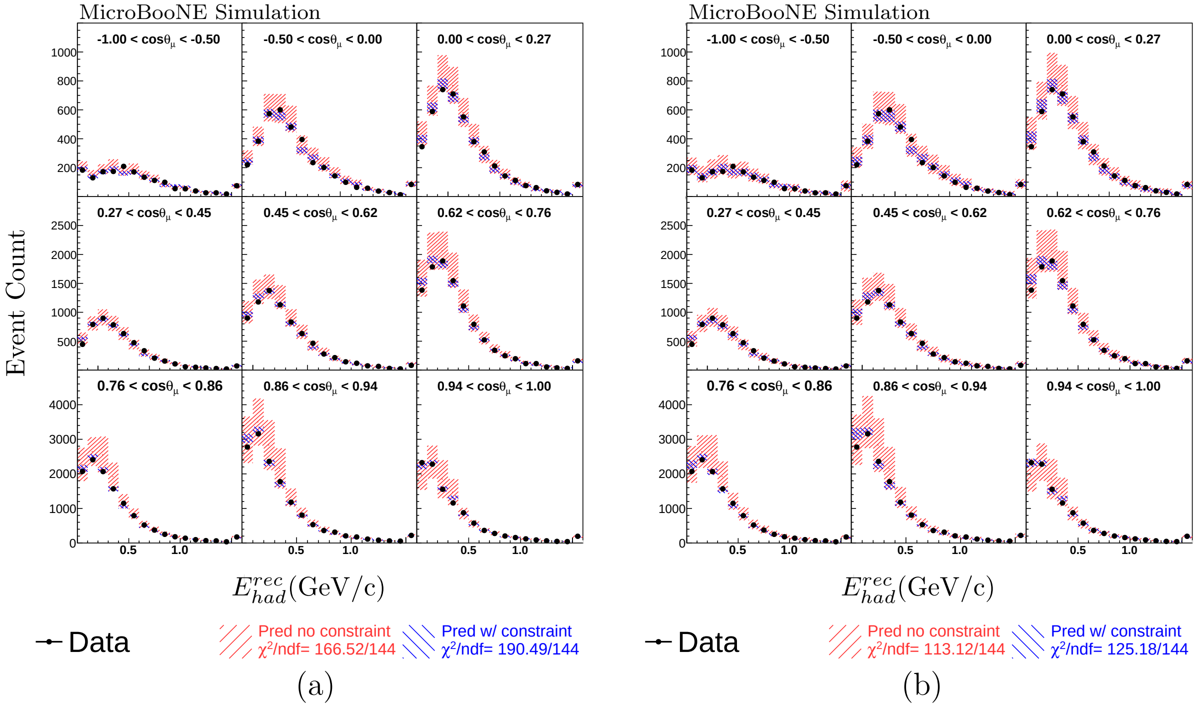

FIG. 7. Comparison on the distribution of partially contained events between `NuWro` fake data and model and prediction using (a) cross section and statistical uncertainties and (b) all uncertainties over the 2D distribution $\{E^{\rm rec}_{\rm had}, \cos(\theta^{\rm rec}_{\mu})\}$. The red (blue) band gives the uncertainty before (after) applying the 2D $\{P^{\rm rec}_{\mu}, \cos(\theta^{\rm rec}_{\mu})\}$ distribution as a constraint on the model prediction following Eq. 10. The statistical and systematic uncertainties of the data and simulation are included in the uncertainty bands shown with the model prediction.

TABLE I. Model validation goodness-of-fit (GoF) tests compared against bias in extracted cross section measurements using the 138 analysis bins of the 3D measurement. Fake data sets are used, consisting of simulation from the `MicroBooNE model` under various proton energy scalings from 70% to 130%. GoF tests are performed on the partially contained $\{E_{\text{had}}^{\text{rec}}, \cos(\theta_\mu^{\text{rec}})\}$ distribution, using the $\{P_\mu^{\text{rec}}, \cos(\theta_\mu^{\text{rec}})\}$ distribution as a constraint.

E_p Scaling (%)	Cross Section & Stat Unc. GoF χ^2 (p-value) 144 DoF	Cross Section & Stat Unc. Cross Section Bias χ^2 (p-value) 138 DoF	All Uncertainties GoF χ^2 (p-value) 144 DoF	All Uncertainties Cross Section Bias χ^2 (p-value) 138 DoF
70	554.6 (2×10^{-49})	240.7 (1.4×10^{-7})	216.4 (9.5×10^{-5})	126.3 (0.753)
75	365.9 (3×10^{-21})	162.1 (0.08)	147.7 (0.40)	85.5 (1)
80	225.4 (1.7×10^{-5})	104.5 (0.985)	95.8 (0.999)	55.5 (1)
85	123.6 (0.89)	60.1 (1)	55.8 (1)	32.6 (1)
90	58.1 (1)	27.4 (1)	29.0 (1)	14.8 (1)
95	17.0 (1)	7.2 (1)	9.2 (1)	3.7 (1)
105	18.7 (1)	7.5 (1)	11.0 (1)	3.8 (1)
110	48.3 (1)	26.8 (1)	26.1 (1)	14.0 (1)
115	96.9 (0.999)	62.3 (1)	52.6 (1)	32.3 (1)
120	152.7 (0.29)	104.3 (0.985)	82.7 (1)	53.7 (1)
125	217.4 (8×10^{-5})	159.2 (0.105)	114.3 (0.967)	81.4 (1)
130	289.5 (9×10^{-12})	229.6 (1.6×10^{-6})	151.4 (0.321)	115.6 (0.917)

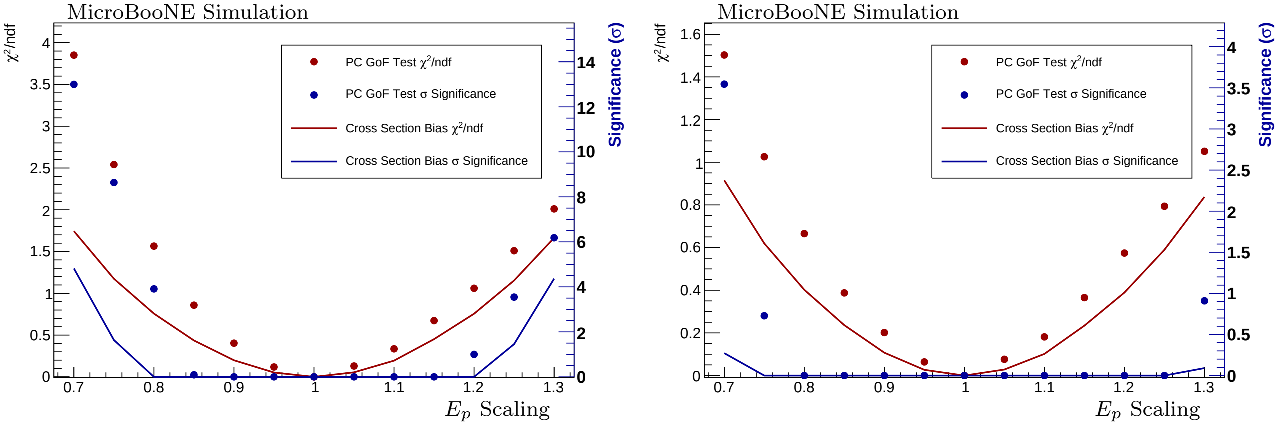

(a)

(b)

FIG. 8. Comparison between GoF test results and extracted cross section bias for various proton energy scalings, using (a) cross section and statistical uncertainties only, and (b) all uncertainties.

The partially contained distribution is highlighted because it is found to be more sensitive to mismodeling than other distributions in these specific fake data studies. In the case of cross section and statistical uncertainties, the constrained GoF tests detect the mismodeling at -20% proton energy with a χ^2/ndf of 225.4/144 and corresponding p-value of 1.7×10^{-5} and at +25% proton energy with a χ^2/ndf of 217.4/144 and corresponding p-value of 8×10^{-5}. Meanwhile, the respective extracted cross sections both demonstrate lower χ^2/ndf ratios and corresponding p-values within 2σ. When all uncertainties are included, the constrained GoF tests begin to detect mismodeling at -25% and +30%, while the extracted cross section remains within uncertainties with corresponding p-values below 2σ across the full range of proton energy scalings. Furthermore, Fig. 8 contains the same information as Table I and visually shows that the GoF tests contain larger χ^2/ndf values and statistical significances than the corresponding extracted cross section for all proton energy scalings under both uncertainty treatments.

IV. FORMATION OF MASTER EQUATION TO UNFOLD THREE-DIMENSIONAL CROSS SECTIONS

In this section we provide the exact mathematical derivation for the cross section unfolding procedure in multiple dimensions. The derivation for the cross section unfolding in the case of one dimension is given in the supplemental material of the previous work [8]. The process of extracting information about the truth content of the measurement bins, given the observed measurements, is referred to as “unfolding.” For a typical data unfolding problem, the formation of the master equation

$$M = R \cdot S \tag{12}$$

is crucial. Here M is the measurable quantity (typically a vector) in the reconstructed kinematics variable space. S is the physics quantity (typically also a vector) to be extracted in the true kinematic variable space, which is the goal of the unfolding procedure. Then the response matrix R, which is assumed to be known, connects the unknown S with the actual measurement M, and can be determined from theoretical modeling or simulation. As discussed in Sec. II, in this work the estimation of R through the use of the MicroBooNE model is extensively validated. This gives confidence that the unfolding performed based on this estimation of R will not introduce bias beyond the uncertainty shown on the measurement.

In this section, we describe the exact formalism to form the master equation (Eq. 12) for the extraction of the three-dimensional cross section on neutrino energy E_ν and two kinematic variables K and P. M represents the measured number of events as a function of the reconstructed neutrino energy E_ν^{rec} and kinematic variables K^{rec} and P^{rec}:

$$M\left(E_\nu^{\mathrm{rec}}, K^{\mathrm{rec}}, P^{\mathrm{rec}}\right) = N \cdot T \cdot \int\int\int F\left(E_\nu\right) \cdot \frac{d^2\sigma\left(E_\nu, K, P\right)}{dKdP} \cdot D \cdot \epsilon \cdot dE_\nu \cdot dK \cdot dP + B\left(E_\nu^{\mathrm{rec}}, K^{\mathrm{rec}}, P^{\mathrm{rec}}\right), \tag{13}$$

where N and T represent the integrated protons on target (POT) and the number of target nucleons respectively. $F\left(E_\nu\right)$ is the muon neutrino flux as a function of true neutrino energy E_ν. The differential cross section $\frac{d^2\sigma(E_\nu,K,P)}{dKdP}$ is a function of true energy E_ν, K and P. The detector response matrix D [or $D\left(E_\nu, E_\nu^{\mathrm{rec}}, K, K^{\mathrm{rec}}, P, P^{\mathrm{rec}}\right)$] is a function of E_ν, E_ν^{rec}, K, K^{rec}, P, and P^{rec}, and represents smearing of the neutrino energy reconstruction. The selection efficiency ϵ [or $\epsilon\left(E_\nu, K, K^{\mathrm{rec}}, P, P^{\mathrm{rec}}\right)$] is a function of E_ν, K, K^{rec}, P, and P^{rec}. The last term, $B\left(E_\nu^{\mathrm{rec}}, K^{\mathrm{rec}}, P^{\mathrm{rec}}\right)$ represents the estimation of backgrounds as a function of E_ν^{rec}, K^{rec}, P^{rec}, and also depends on N, T, F, σ, and the selection strategy.

We can rewrite Eq. (13) in a matrix format:

$$M_{ijk} = \sum_{lmn} \widetilde{S}_{ijklmn} + B_{ijk}, \tag{14}$$

where i, j, k are bin indices in $E_\nu^{\mathrm{rec}}, K^{\mathrm{rec}}$, and P^{rec}, respectively. Similarly, l, m, n are bin indices in true spaces of E_ν, K, and P. $\widetilde{S}_{ijklmn}$ is the truth signal corresponding to bin lmn and reconstructed in bin ijk.

$$\begin{aligned}
\widetilde{S}_{ijklmn} &= \frac{N \cdot T \cdot \int_{lmn} F\left(E_{\nu\ l}\right) \cdot \frac{d^2\sigma\left(E_{\nu\ l}, K_m, P_n\right)}{dK_m dP_n} \cdot D \cdot \epsilon \cdot dE_{\nu\ l} \cdot dK_m \cdot dP_n}{N \cdot T \cdot \int_{lmn} \overline{F}\left(E_{\nu\ l}\right) \cdot \frac{d^2\sigma\left(E_{\nu\ l}, K_m, P_n\right)}{dK_m dP_n} \cdot dE_{\nu\ l} \cdot dK_m \cdot dP_n} \\
&\cdot \left(N \cdot T \cdot \int_{lmn} \overline{F}\left(E_{\nu\ l}\right) \cdot dE_{\nu\ l} \cdot dK_m \cdot dP_n\right) \\
&\cdot \frac{\int_{lmn} \overline{F}\left(E_{\nu\ l}\right) \cdot \frac{d^2\sigma\left(E_{\nu\ l}, K_m, P_n\right)}{dK_m dP_n} \cdot dE_{\nu\ l} \cdot dK_m \cdot dP_n}{\int_{lmn} \overline{F}\left(E_{\nu\ l}\right) \cdot dE_{\nu\ l} \cdot dK_m \cdot dP_n} \\
&= \Delta_{ijklmn} \cdot F_{lmn} \cdot S_{lmn},
\end{aligned} \tag{15}$$

with

$$\Delta_{ijklmn} \equiv \frac{N \cdot T \cdot \int_{lmn} F\left(E_{\nu\ l}\right) \cdot \frac{d^2\sigma\left(E_{\nu\ l}, K_m, P_n\right)}{dK_m dP_n} \cdot D \cdot \epsilon \cdot dE_{\nu\ l} \cdot dK_m \cdot dP_n}{N \cdot T \cdot \int_{lmn} \overline{F}\left(E_\nu\right) \cdot \frac{d^2\sigma\left(E_{\nu\ l}, K_m, P_n\right)}{dK_m dP_n} \cdot dE_\nu \cdot dK_m \cdot dP_n} \tag{16}$$

being the smearing matrix that can be directly extracted from the simulation:

$$\Delta_{ijklmn} = \frac{\text{Selected no. of events in reco. bin } (i, j, k) \text{ from true bin } (l, m, n) \text{ after event weights}}{\text{Generated no. of events in true bin } (l, m, n) \text{ after event weights}}, \tag{17}$$

which is also used to estimate the impact of various systematic uncertainties (e.g. neutrino flux, neutrino-argon interaction cross section, and detector systematics). Here $\overline{F}$ represents the nominal (or central value) estimation of the ν_μ neutrino flux. Furthermore,

$$\begin{aligned}
F_{lmn} &\equiv N \cdot T \cdot \int_{lmn} \overline{F}\left(E_{\nu\ l}\right) \cdot dE_{\nu\ l} \cdot dK_m \cdot dP_n \\
&= N \cdot T \cdot \left(\int_l \overline{F}\left(E_{\nu\ l}\right) \cdot dE_{\nu\ l}\right) \cdot \Delta K_m \cdot \Delta P_n
\end{aligned} \tag{18}$$

is a constant that can be calculated externally knowing the nominal ν_μ neutrino flux, the m-th bin width ΔK_m and the n-th bin width ΔP_n. Finally, the targeted signal to be unfolded is defined as:

$$\begin{aligned} S_j &\equiv \frac{\int_{lmn} \overline{F}\left(E_{\nu\ l}\right) \cdot \frac{d^2\sigma(E_{\nu\ l},K_m,P_n)}{dK_m dP_n} \cdot dE_{\nu\ l} \cdot dK_m \cdot dP_n}{\int_{lmn} \overline{F}\left(E_{\nu\ l}\right) \cdot dE_{\nu\ l} \cdot dK_m \cdot dP_n} \\ &= \left\langle \frac{d^2\sigma\left(E_{\nu,l},K_m,P_n\right)}{dK_m dP_n} \right\rangle, \end{aligned} \tag{19}$$

and is the flux-averaged three-dimensional cross section of true neutrino energy bin l, true K bin m and true P bin n that we pursue in the unfolding procedure. Mapping $R_{ijklmn} = \Delta_{ijklmn} \cdot F_{lmn}$ to Eq. (14), we have

$$M_{ijk} - B_{ijk} = \sum_{lmn} R_{ijklmn} \cdot S_{lmn}. \tag{20}$$

One can concatenate the three indices, and remap ijk and lmn to i and j, respectively. As a result, we have

$$M_i - B_i = \sum_j R_{ij} \cdot S_j, \tag{21}$$

which is essentially the master equation in Eq. (12).

V. CROSS SECTION RESULT DATA RELEASE

The data are compared against each model prediction within individual E_ν slices, with χ^2 values shown in Table II and Table III. The extracted ν_μ CC differential inclusive scattering cross section per argon nucleus as a function of neutrino energy, $d^2\sigma(E_\nu)/d\cos(\theta_\mu)dP_\mu$, is provided in the included root file `microboone_cc_inclusive_cross_section.root` and text file `microboone_cc_inclusive_cross_section.txt`, and in Table IV. The bin ranges over E_ν, $\cos(\theta_\mu)$, and P_μ are also included. The nominal BNB flux is available in the supplemental material of Ref. [10]. The covariance matrix and additional smearing matrix are provided in the included text files `microboone_cc_inclusive_cov_matrix.txt` and `microboone_cc_inclusive_additional_smearing_matrix.txt`, respectively. The covariance matrix is also shown in Fig. 9, consisting of both statistical and systematic uncertainties and given in units of $(10^{-36}\ \mathrm{cm}^2/\mathrm{GeV}/\mathrm{Ar})^2$. The additional smearing is a result of the regularization in the data unfolding procedure, and should be applied to model predictions when comparing to these cross-section results. Figure 10 shows the three-dimensional cross section measurement plotted against the `MicroBooNE model` prediction. Figure 11 shows the data over the two-dimensional distribution of $\{E_\nu, \cos(\theta_\mu)\}$, plotted against the `NuWro` model prediction, with a breakdown of the predicted contributions from different interaction channels. This distribution is constructed from the three-dimensional measurement by integrating over P_μ and normalizing by the average neutrino energy $\langle E_\nu \rangle$.

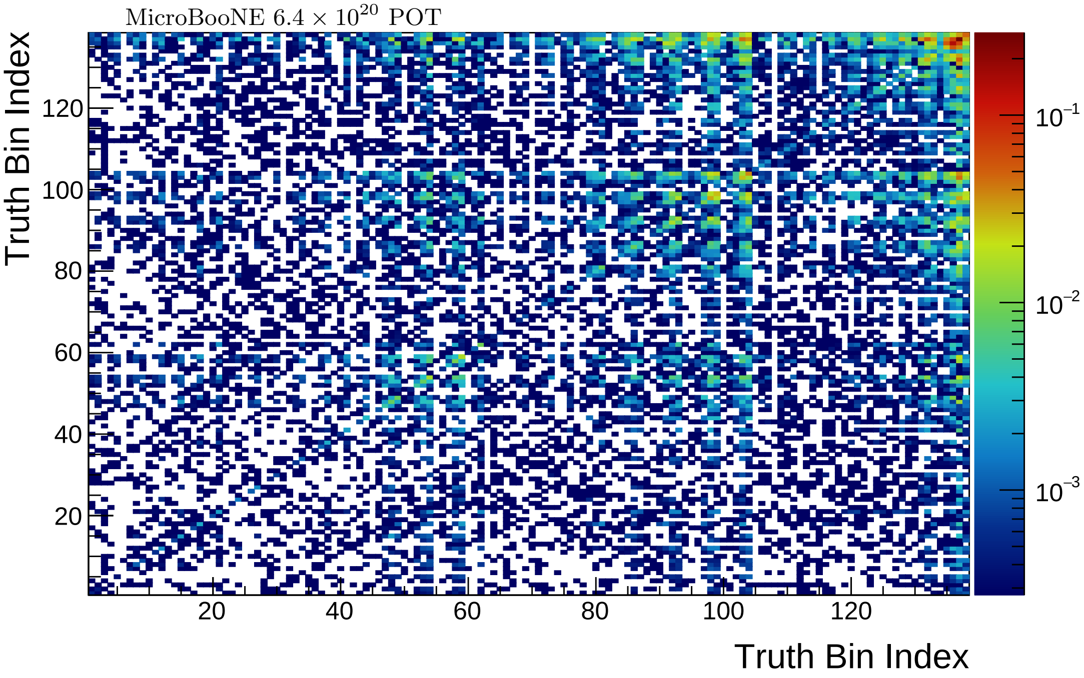

FIG. 9. Covariance matrix showing total statistical plus systematic uncertainties over the 138 measurement bins, in units of $(10^{-36}\ \mathrm{cm}^2/\mathrm{GeV}/\mathrm{Ar})^2$. Bins with extremely low values are colored white.

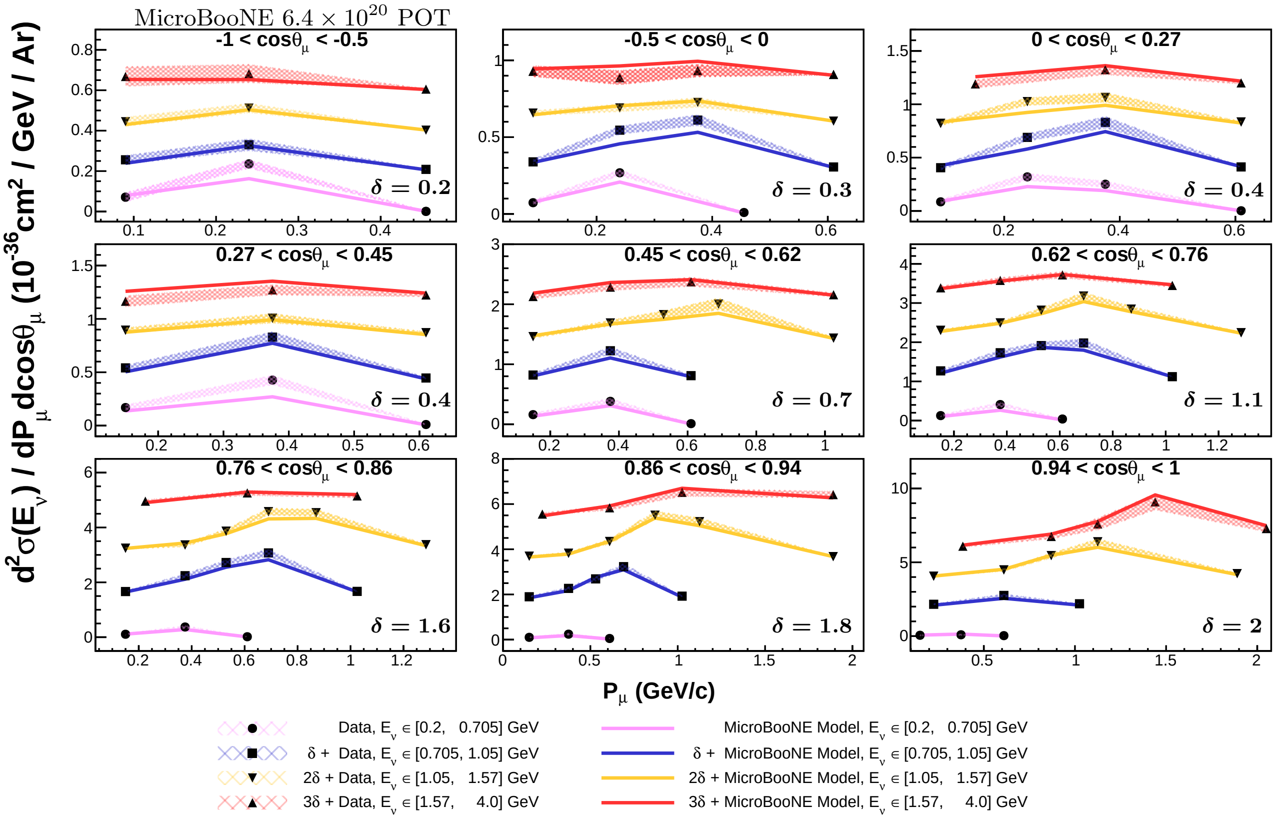

FIG. 10. Unfolded measurement of the inclusive ν_μCC differential cross section on argon and `MicroBooNE model` prediction are shown within each angle slice and with each E_ν measurement overlaid and offset to visually separate them. The magnitude of the offset δ, given in the same units as the cross section, $10^{-36}\mathrm{cm}^2/\mathrm{GeV}/\mathrm{Ar}$, is shown in the bottom right of each plot. Uncertainties on the extracted cross section are shown through the shaded bands.

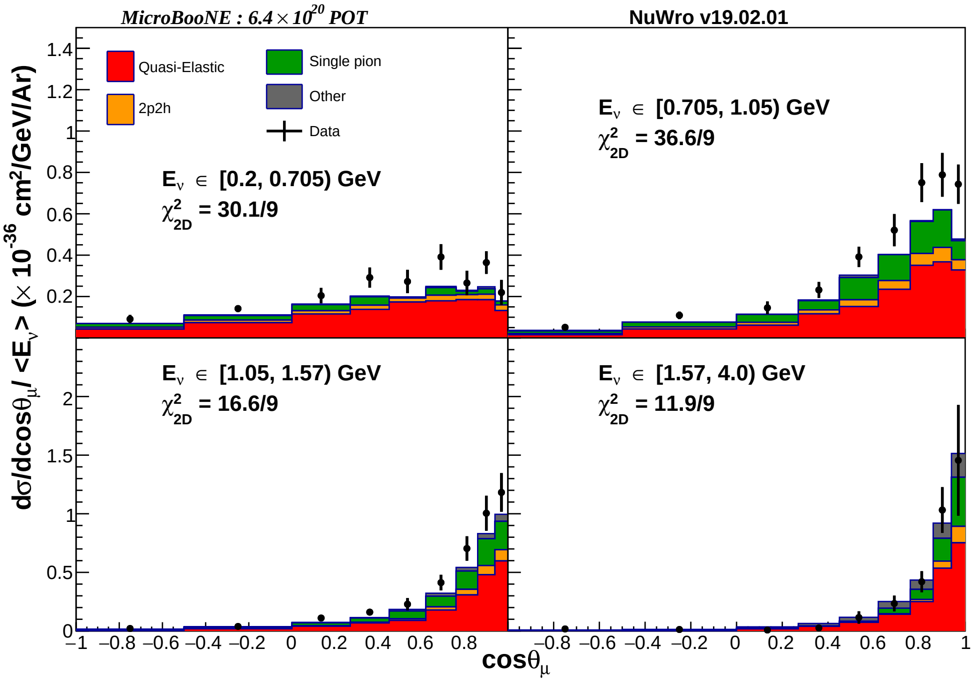

FIG. 11. Unfolded differential cross section over a function of $\cos(\theta_\mu)$ after integrating over P_μ and normalizing by the average $\langle E_\nu \rangle$ in each E_ν bin. The `NuWro` prediction, including a breakdown of interaction channel, is given for comparison.

TABLE II. Comparisons between various models and the unfolded three-dimensional measurement within each E_ν slice.

Model Name	Total χ^2/ndf	$[0.2, 0.705]$ GeV χ^2/ndf	$[0.705, 1.05]$ GeV χ^2/ndf	$[1.05, 1.57]$ GeV χ^2/ndf	$[1.57, 4.0]$ GeV χ^2/ndf
`GENIE v2`	752.2/138	69.3/28	61.3/35	63.0/42	34.9/33
`MicroBooNE model`	329.3/138	88.0/28	77.7/35	43.5/42	31.1/33
`GENIE v3 untuned`	324.6/138	101.2/28	85.2/35	50.2/42	36.4/33
`GiBUU`	275.2/138	36.0/28	48.7/35	53.8/42	29.6/33
`NEUT`	244.3/138	65.3/28	58.7/35	40.8/42	37.0/33
`NuWro`	214.1/138	60.8/28	65.8/35	40.3/42	28.8/33

TABLE III. Comparisons between various models and the unfolded three-dimensional measurement within each E_ν slice after integrating over the P_μ dimension.

Model Name	Total χ^2/ndf	$[0.2, 0.705]$ GeV χ^2/ndf	$[0.705, 1.05]$ GeV χ^2/ndf	$[1.05, 1.57]$ GeV χ^2/ndf	$[1.57, 4.0]$ GeV χ^2/ndf
`GENIE v2`	125.5/36	12.5/9	16.6/9	20.7/9	12.7/9
`MicroBooNE model`	87.0/36	36.5/9	34.8/9	12.3/9	12.2/9
`GENIE v3 untuned`	99.9/36	57.3/9	55.0/9	28.1/9	14.0/9
`GiBUU`	95.5/36	11.4/9	13.0/9	14.6/9	10.3/9
`NEUT`	70.5/36	32.5/9	28.4/9	6.8/9	16.4/9
`NuWro`	75.6/36	30.1/9	36.6/9	16.6/9	11.9/9

TABLE IV: ν_μ CC inclusive differential cross section per argon atom in each neutrino energy bin with total statistical plus systematic uncertainty. The total uncertainty comes from the square root of the covariance matrix diagonal entries.

Bin Number	E_ν Range [GeV]	$\cos(\theta_\mu)$ Range	P_μ Range [GeV]	σ_{MC} [10^{-36} cm^2/GeV/Ar]	σ_{Data} [10^{-36} cm^2/GeV/Ar]	Total Uncertainty [10^{-36} cm^2/Ar]
0	[0.2, 0.705]	[-1, -0.5]	[0, 0.18]	0.079	0.071	0.023
1	[0.2, 0.7]	[-1, -0.5]	[0.18, 0.3]	0.16	0.24	0.022
2	[0.2, 0.7]	[-1, -0.5]	[0.3, 2.5]	0.0012	0.00064	0.0012
3	[0.2, 0.7]	[-0.5, 0]	[0, 0.18]	0.077	0.073	0.017
4	[0.2, 0.7]	[-0.5, 0]	[0.18, 0.3]	0.21	0.27	0.020
5	[0.2, 0.7]	[-0.5, 0]	[0.3, 2.5]	0.0066	0.0094	0.0010
6	[0.2, 0.7]	[0, 0.27]	[0, 0.18]	0.091	0.086	0.022
7	[0.2, 0.7]	[0, 0.27]	[0.18, 0.3]	0.23	0.32	0.035
8	[0.2, 0.7]	[0, 0.27]	[0.3, 0.45]	0.19	0.25	0.031
9	[0.2, 0.7]	[0, 0.27]	[0.45, 2.5]	0.0015	0.0019	0.0022
10	[0.2, 0.7]	[0.27, 0.45]	[0, 0.3]	0.14	0.17	0.026
11	[0.2, 0.7]	[0.27, 0.45]	[0.3, 0.45]	0.27	0.43	0.046
12	[0.2, 0.7]	[0.27, 0.45]	[0.45, 2.5]	0.0069	0.010	0.0039
13	[0.2, 0.7]	[0.45, 0.62]	[0, 0.3]	0.14	0.16	0.029
14	[0.2, 0.7]	[0.45, 0.62]	[0.3, 0.45]	0.31	0.38	0.050
15	[0.2, 0.7]	[0.45, 0.62]	[0.45, 2.5]	0.0050	0.011	0.0049
16	[0.2, 0.7]	[0.62, 0.76]	[0, 0.3]	0.10	0.13	0.031
17	[0.2, 0.7]	[0.62, 0.76]	[0.3, 0.45]	0.26	0.41	0.055
18	[0.2, 0.7]	[0.62, 0.76]	[0.45, 2.5]	0.019	0.040	0.0055
19	[0.2, 0.7]	[0.76, 0.86]	[0, 0.3]	0.11	0.11	0.031
20	[0.2, 0.7]	[0.76, 0.86]	[0.3, 0.45]	0.28	0.37	0.052
21	[0.2, 0.7]	[0.76, 0.86]	[0.45, 2.5]	0.012	0.017	0.0051
22	[0.2, 0.7]	[0.86, 0.94]	[0, 0.3]	0.081	0.10	0.024
23	[0.2, 0.7]	[0.86, 0.94]	[0.3, 0.45]	0.18	0.24	0.041
24	[0.2, 0.7]	[0.86, 0.94]	[0.45, 2.5]	0.024	0.050	0.0060
25	[0.2, 0.7]	[0.94, 1]	[0, 0.3]	0.069	0.060	0.034
26	[0.2, 0.7]	[0.94, 1]	[0.3, 0.45]	0.14	0.092	0.045
27	[0.2, 0.7]	[0.94, 1]	[0.45, 2.5]	0.018	0.034	0.0055
28	[0.7, 1.1]	[-1, -0.5]	[0, 0.18]	0.039	0.056	0.021
29	[0.7, 1.1]	[-1, -0.5]	[0.18, 0.3]	0.13	0.13	0.029
30	[0.7, 1.1]	[-1, -0.5]	[0.3, 2.5]	0.0064	0.0085	0.0026
31	[0.7, 1.1]	[-0.5, 0]	[0, 0.18]	0.035	0.039	0.018

32	[0.7, 1.1]	[-0.5, 0]	[0.18, 0.3]	0.16	0.25	0.027
33	[0.7, 1.1]	[-0.5, 0]	[0.3, 0.45]	0.23	0.31	0.036
34	[0.7, 1.1]	[-0.5, 0]	[0.45, 2.5]	0.0031	0.0058	0.0018
35	[0.7, 1.1]	[0, 0.27]	[0, 0.18]	0.026	0.0053	0.021
36	[0.7, 1.1]	[0, 0.27]	[0.18, 0.3]	0.18	0.29	0.035
37	[0.7, 1.1]	[0, 0.27]	[0.3, 0.45]	0.34	0.43	0.055
38	[0.7, 1.1]	[0, 0.27]	[0.45, 2.5]	0.015	0.013	0.0050
39	[0.7, 1.1]	[0.27, 0.45]	[0, 0.3]	0.10	0.14	0.026
40	[0.7, 1.1]	[0.27, 0.45]	[0.3, 0.45]	0.37	0.43	0.050
41	[0.7, 1.1]	[0.27, 0.45]	[0.45, 2.5]	0.038	0.046	0.0089
42	[0.7, 1.1]	[0.45, 0.62]	[0, 0.3]	0.11	0.12	0.030
43	[0.7, 1.1]	[0.45, 0.62]	[0.3, 0.45]	0.41	0.53	0.060
44	[0.7, 1.1]	[0.45, 0.62]	[0.45, 2.5]	0.092	0.11	0.012
45	[0.7, 1.1]	[0.62, 0.76]	[0, 0.3]	0.11	0.17	0.032
46	[0.7, 1.1]	[0.62, 0.76]	[0.3, 0.45]	0.52	0.63	0.072
47	[0.7, 1.1]	[0.62, 0.76]	[0.45, 0.61]	0.77	0.81	0.096
48	[0.7, 1.1]	[0.62, 0.76]	[0.61, 0.77]	0.70	0.88	0.10
49	[0.7, 1.1]	[0.62, 0.76]	[0.77, 2.5]	0.018	0.021	0.0082
50	[0.7, 1.1]	[0.76, 0.86]	[0, 0.3]	0.047	0.065	0.022
51	[0.7, 1.1]	[0.76, 0.86]	[0.3, 0.45]	0.51	0.64	0.073
52	[0.7, 1.1]	[0.76, 0.86]	[0.45, 0.61]	0.95	1.1	0.095
53	[0.7, 1.1]	[0.76, 0.86]	[0.61, 0.77]	1.2	1.5	0.13
54	[0.7, 1.1]	[0.76, 0.86]	[0.77, 2.5]	0.054	0.070	0.015
55	[0.7, 1.1]	[0.86, 0.94]	[0, 0.3]	0.053	0.097	0.025
56	[0.7, 1.1]	[0.86, 0.94]	[0.3, 0.45]	0.37	0.47	0.060
57	[0.7, 1.1]	[0.86, 0.94]	[0.45, 0.61]	0.96	0.89	0.10
58	[0.7, 1.1]	[0.86, 0.94]	[0.61, 0.77]	1.3	1.4	0.13
59	[0.7, 1.1]	[0.86, 0.94]	[0.77, 2.5]	0.082	0.12	0.020
60	[0.7, 1.1]	[0.94, 1]	[0, 0.45]	0.095	0.16	0.035
61	[0.7, 1.1]	[0.94, 1]	[0.45, 0.77]	0.56	0.76	0.10
62	[0.7, 1.1]	[0.94, 1]	[0.77, 2.5]	0.10	0.19	0.020
63	[1.1, 1.6]	[-1, -0.5]	[0, 0.18]	0.030	0.044	0.023
64	[1.1, 1.6]	[-1, -0.5]	[0.18, 0.3]	0.10	0.11	0.023
65	[1.1, 1.6]	[-1, -0.5]	[0.3, 2.5]	0.0031	0.0025	0.0019
66	[1.1, 1.6]	[-0.5, 0]	[0, 0.18]	0.046	0.057	0.017
67	[1.1, 1.6]	[-0.5, 0]	[0.18, 0.3]	0.10	0.090	0.025
68	[1.1, 1.6]	[-0.5, 0]	[0.3, 0.45]	0.14	0.13	0.032
69	[1.1, 1.6]	[-0.5, 0]	[0.45, 2.5]	0.0047	0.0043	0.0023
70	[1.1, 1.6]	[0, 0.27]	[0, 0.18]	0.033	0.021	0.021
71	[1.1, 1.6]	[0, 0.27]	[0.18, 0.3]	0.12	0.22	0.036
72	[1.1, 1.6]	[0, 0.27]	[0.3, 0.45]	0.19	0.26	0.046
73	[1.1, 1.6]	[0, 0.27]	[0.45, 2.5]	0.025	0.034	0.0060
74	[1.1, 1.6]	[0.27, 0.45]	[0, 0.3]	0.075	0.094	0.024
75	[1.1, 1.6]	[0.27, 0.45]	[0.3, 0.45]	0.19	0.21	0.045
76	[1.1, 1.6]	[0.27, 0.45]	[0.45, 2.5]	0.053	0.070	0.0099
77	[1.1, 1.6]	[0.45, 0.62]	[0, 0.3]	0.076	0.060	0.027
78	[1.1, 1.6]	[0.45, 0.62]	[0.3, 0.45]	0.27	0.29	0.048
79	[1.1, 1.6]	[0.45, 0.62]	[0.45, 0.61]	0.35	0.43	0.064
80	[1.1, 1.6]	[0.45, 0.62]	[0.61, 0.77]	0.45	0.60	0.097
81	[1.1, 1.6]	[0.45, 0.62]	[0.77, 2.5]	0.032	0.036	0.013
82	[1.1, 1.6]	[0.62, 0.76]	[0, 0.3]	0.076	0.10	0.025
83	[1.1, 1.6]	[0.62, 0.76]	[0.3, 0.45]	0.28	0.29	0.045
84	[1.1, 1.6]	[0.62, 0.76]	[0.45, 0.61]	0.53	0.62	0.060
85	[1.1, 1.6]	[0.62, 0.76]	[0.61, 0.77]	0.84	0.98	0.096
86	[1.1, 1.6]	[0.62, 0.76]	[0.77, 0.97]	0.58	0.64	0.072
87	[1.1, 1.6]	[0.62, 0.76]	[0.97, 2.5]	0.030	0.042	0.016
88	[1.1, 1.6]	[0.76, 0.86]	[0, 0.3]	0.037	0.044	0.030
89	[1.1, 1.6]	[0.76, 0.86]	[0.3, 0.45]	0.23	0.16	0.067
90	[1.1, 1.6]	[0.76, 0.86]	[0.45, 0.61]	0.57	0.66	0.083
91	[1.1, 1.6]	[0.76, 0.86]	[0.61, 0.77]	1.1	1.4	0.13
92	[1.1, 1.6]	[0.76, 0.86]	[0.77, 0.97]	1.1	1.3	0.13
93	[1.1, 1.6]	[0.76, 0.86]	[0.97, 2.5]	0.14	0.17	0.031
94	[1.1, 1.6]	[0.86, 0.94]	[0, 0.3]	0.056	0.092	0.024
95	[1.1, 1.6]	[0.86, 0.94]	[0.3, 0.45]	0.19	0.22	0.048

96	[1.1, 1.6]	[0.86, 0.94]	[0.45, 0.77]	0.75	0.74	0.10
97	[1.1, 1.6]	[0.86, 0.94]	[0.77, 0.97]	1.8	1.9	0.18
98	[1.1, 1.6]	[0.86, 0.94]	[0.97, 1.3]	1.4	1.6	0.17
99	[1.1, 1.6]	[0.86, 0.94]	[1.3, 2.5]	0.075	0.074	0.022
100	[1.1, 1.6]	[0.94, 1]	[0, 0.45]	0.068	0.058	0.039
101	[1.1, 1.6]	[0.94, 1]	[0.45, 0.77]	0.53	0.48	0.082
102	[1.1, 1.6]	[0.94, 1]	[0.77, 0.97]	1.5	1.5	0.17
103	[1.1, 1.6]	[0.94, 1]	[0.97, 1.3]	2.0	2.4	0.20
104	[1.1, 1.6]	[0.94, 1]	[1.3, 2.5]	0.17	0.23	0.034
105	[1.6, 4]	[-1, -0.5]	[0, 0.18]	0.053	0.068	0.049
106	[1.6, 4]	[-1, -0.5]	[0.18, 0.3]	0.053	0.083	0.045
107	[1.6, 4]	[-1, -0.5]	[0.3, 2.5]	0.0035	0.0055	0.0019
108	[1.6, 4]	[-0.5, 0]	[0, 0.18]	0.044	0.029	0.036
109	[1.6, 4]	[-0.5, 0]	[0.18, 0.3]	0.063	-0.012	0.046
110	[1.6, 4]	[-0.5, 0]	[0.3, 0.45]	0.094	0.033	0.041
111	[1.6, 4]	[-0.5, 0]	[0.45, 2.5]	0.0027	0.0079	0.0043
112	[1.6, 4]	[0, 0.27]	[0, 0.3]	0.058	-0.0092	0.039
113	[1.6, 4]	[0, 0.27]	[0.3, 0.45]	0.16	0.12	0.048
114	[1.6, 4]	[0, 0.27]	[0.45, 2.5]	0.017	0.00036	0.011
115	[1.6, 4]	[0.27, 0.45]	[0, 0.3]	0.059	-0.034	0.051
116	[1.6, 4]	[0.27, 0.45]	[0.3, 0.45]	0.15	0.072	0.049
117	[1.6, 4]	[0.27, 0.45]	[0.45, 2.5]	0.042	0.025	0.017
118	[1.6, 4]	[0.45, 0.62]	[0, 0.3]	0.085	0.029	0.042
119	[1.6, 4]	[0.45, 0.62]	[0.3, 0.45]	0.26	0.19	0.057
120	[1.6, 4]	[0.45, 0.62]	[0.45, 0.77]	0.31	0.27	0.076
121	[1.6, 4]	[0.45, 0.62]	[0.77, 2.5]	0.052	0.058	0.032
122	[1.6, 4]	[0.62, 0.76]	[0, 0.3]	0.067	0.088	0.048
123	[1.6, 4]	[0.62, 0.76]	[0.3, 0.45]	0.26	0.28	0.071
124	[1.6, 4]	[0.62, 0.76]	[0.45, 0.77]	0.43	0.42	0.083
125	[1.6, 4]	[0.62, 0.76]	[0.77, 2.5]	0.17	0.15	0.044
126	[1.6, 4]	[0.76, 0.86]	[0, 0.45]	0.11	0.16	0.050
127	[1.6, 4]	[0.76, 0.86]	[0.45, 0.77]	0.49	0.46	0.095
128	[1.6, 4]	[0.76, 0.86]	[0.77, 2.5]	0.40	0.35	0.069
129	[1.6, 4]	[0.86, 0.94]	[0, 0.45]	0.079	0.16	0.058
130	[1.6, 4]	[0.86, 0.94]	[0.45, 0.77]	0.52	0.44	0.11
131	[1.6, 4]	[0.86, 0.94]	[0.77, 1.3]	1.3	1.1	0.18
132	[1.6, 4]	[0.86, 0.94]	[1.3, 2.5]	0.88	1.0	0.15
133	[1.6, 4]	[0.94, 1]	[0, 0.77]	0.16	0.089	0.073
134	[1.6, 4]	[0.94, 1]	[0.77, 0.97]	0.91	0.75	0.17
135	[1.6, 4]	[0.94, 1]	[0.97, 1.3]	1.8	1.6	0.40
136	[1.6, 4]	[0.94, 1]	[1.3, 1.6]	3.6	3.1	0.55
137	[1.6, 4]	[0.94, 1]	[1.6, 2.5]	1.5	1.3	0.23

[1] C. Rasmussen *et al.*, *Gaussian Processes for Machine Learning (Adaptive Computation and Machine Learning)* (The MIT Press, 2005).

[2] M. Frate *et al.*, Modeling Smooth Backgrounds and Generic Localized Signals with Gaussian Processes, (2017), arXiv:1709.05681 [physics.data-an].

[3] L. Li *et al.*, Efficient neutrino oscillation parameter inference using Gaussian processes, Phys. Rev. D **101**, 012001 (2020).

[4] P. Abratenko *et al.* (MicroBooNE Collaboration), Search for an anomalous excess of inclusive charged-current ν_e interactions in the MicroBooNE experiment using Wire-Cell reconstruction, Phys. Rev. D **105**, 112005 (2022).

[5] P. Abratenko *et al.* (MicroBooNE Collaboration), Novel approach for evaluating detector-related uncertainties in a LArTPC using MicroBooNE data, The Eur. Phys. J. C **82**, 454 (2022).

[6] P. Abratenko *et al.* (MicroBooNE Collaboration), First Simultaneous Measurement of Differential Muon-Neutrino Charged-Current Cross Sections on Argon for Final States with and without Protons Using MicroBooNE Data, Phys. Rev. Lett. **133**, 041801 (2024).

[7] M. Eaton, Multivariate statistics: a vector space approach, John Wiley and Sons , 116 (1983).

[8] P. Abratenko *et al.* (MicroBooNE Collaboration), First Measurement of Energy-Dependent Inclusive Muon Neutrino Charged-Current Cross Sections on Argon with the MicroBooNE Detector, Phys. Rev. Lett. **128**, 151801 (2022).

[9] P. Abratenko *et al.* (MicroBooNE Collaboration), Inclusive cross section measurements in final states with and without protons for charged-current ν_μ-Ar scattering in MicroBooNE, Phys. Rev. D **110**, 013006 (2024).

[10] P. Abratenko *et al.* (MicroBooNE Collaboration), First Measurement of Inclusive Muon Neutrino Charged Current Differential Cross Sections on Argon at $E_\nu \sim 0.8$ GeV with the MicroBooNE Detector, Phys. Rev. Lett. **123**, 131801 (2019), arXiv:1905.09694.